COMPACT H I CLOUDS FROM THE GALFA-H I SURVEY

AYESHA BEGUM[1], SNEŽANA STANIMIROVIĆ[1], JOSHUA E. PEEK[2], NICHOLAS P. BALLERING[1], CARL HEILES[3], KEVIN A. DOUGLAS[4],
MARY PUTMAN[2], STEVEN J. GIBSON[5], JANA GRCEVICH[2], ERIC J. KORPELA[6], MIN-YOUNG LEE[1], DESTRY SAUL[2],
AND JOHN S. GALLAGHER III[1]
[1] University of Wisconsin, Madison, 475 North Charter Street, Madison, WI 53703, USA; sstanimi@astro.wisc.edu
[2] Department of Astronomy, Columbia University, New York, NY 10027, USA
[3] Radio Astronomy Laboratory, UC Berkeley, 601 Campbell Hall, Berkeley, CA 94720, USA; heiles@astro.berkeley.edu
[4] School of Physics, University of Exeter, Stocker Road, Exeter, EX4 4QL, UK
[5] Department of Physics and Astronomy, Western Kentucky University, Bowling Green, KY 42101, USA
[6] Space Sciences Laboratory, University of California, Berkeley, CA 94720, USA

ABSTRACT

The Galactic Arecibo *L*-band Feed Array H I (GALFA-H I) survey is mapping the entire Arecibo sky at 21 cm, over a velocity range of -700 to $+700$ km s^{-1} (LSR), at a velocity resolution of 0.18 km s^{-1}, and a spatial resolution of 3.5 arcmin. The unprecedented resolution and sensitivity of the GALFA-H I survey have resulted in the detection of numerous isolated, very compact H I clouds at low Galactic velocities, which are distinctly separated from the H I disk emission. In the limited area of $\sim$4600 deg^2 surveyed so far, we have detected 96 such compact clouds. The detected clouds are cold with a median $T_{k,\max}$ (the kinetic temperature in the case in which there is no non-thermal broadening) of 300 K. Moreover, these clouds are quite compact and faint, with median values of 5 arcmin in angular size, 0.75 K in peak brightness temperature, and 5×10^{18} cm^{-2} in H I column density. Most of the clouds deviate from Galactic rotation at the 20–30 km s^{-1} level, and a significant fraction show evidence for a multiphase medium and velocity gradients. No counterparts for these clouds were found in other wave bands. From the modeling of spatial and velocity distributions of the whole compact cloud population, we find that the bulk of the compact clouds are related to the Galactic disk, and their distances are likely to be in the range of 0.1 to a few kpc. We discuss various possible scenarios for the formation and maintenance of this cloud population and its significance for Galactic interstellar medium studies.

Key words: Galaxy: evolution – Galaxy: halo – ISM: clouds – ISM: kinematics and dynamics – ISM: structure – radio lines: ISM

1. INTRODUCTION

The neutral interstellar medium (ISM) is known to exist in two thermal equilibrium states: the cold neutral medium (CNM) and the warm neutral medium (WNM; Field et al. 1969; McKee & Ostriker 1977; Wolfire et al. 2003). Both the CNM and the WNM are highly structured over a range of spatial scales, and exhibit a variety of morphologies including sheets, filaments, shells, and clouds (Kalberla & Kerp 2009). The 21 cm line of neutral hydrogen (H I) has been the main tracer of the multiphase neutral ISM in the Galactic thin disk and beyond. The disk–halo interface region, extending up to 1–1.5 kpc above the disk and interfacing with the Galactic halo gas, was initially considered to represent a smooth envelope of H I surrounding the Galactic spiral structure. However, with the improvement in sensitivity and spatial resolution of the Galactic surveys, discrete H I clouds have been detected down to a scale of a few parsecs (Lockman 2002; Stil et al. 2006a; Stanimirović et al. 2006; Ford et al. 2008).

Traditionally, H I observations have been able to trace the entire hierarchy of structures in the neutral ISM on scales $\geqslant$1 pc. However, the small-scale end of this spectrum, i.e., scales $<$ pc, is still largely unexplored because of a paucity of high spatial/velocity resolution imaging surveys. Cold H I structures have been observed on sub-parsec scales, predominantly within the Galactic plane, as H I self-absorption (HISA) features against the extended background of the WNM (Gibson et al. 2005). On the other hand, detection of the smallest H I structures down to tens of astronomical units mainly relies on the absorption measurements against continuum background sources, or from the time variability of H I absorption profiles against pulsars (Frail et al. 1994; Heiles 1997; Stanimirović et al. 2007). Regarding the sub-parsec scale structure of the Galactic disk–halo interface region, several studies have been conducted by mapping the H I gas in emission using interferometers. However, such studies require a substantial investment of telescope time, hence have been mainly limited to small, targeted regions in the Galaxy (Stil et al. 2006b; Dedes et al. 2008; Bekhti et al. 2009; Dedes & Kalberla 2010).

The presence of sub-parsec scale clouds in the ISM raises many important questions. For example, how abundant is this cloud population? What are the formation and survival mechanisms for such clouds? Also, what role do these clouds play in the general ISM? In addition, such clouds are fascinating because they may be related to major dynamical processes in the ISM such as stellar winds (Matthews et al. 2008; Gerard & Le Bertre 2006), shocks (Gibson et al. 2005), turbulence (Vazquez-Semadeni et al. 2006; de Avillez & Breitschwerdt 2005; Audit & Hennebelle 2005), and Galactic accretion (Heitsch & Putman 2009). To fully investigate the nature of small-scale H I structure a sensitive, unbiased, high-resolution survey of the entire sky is required.

The Galactic Arecibo *L*-band Feed Array H I (GALFA-H I) survey is successfully mapping the entire Arecibo sky at 21 cm. The survey covers a velocity range of -700 to $+700$ km s^{-1} (LSR) at an unprecedented velocity resolution of 0.18 km s^{-1} and a spatial resolution of 3.5 arcmin. The combination of sensitivity and resolution provided by the GALFA-H I survey
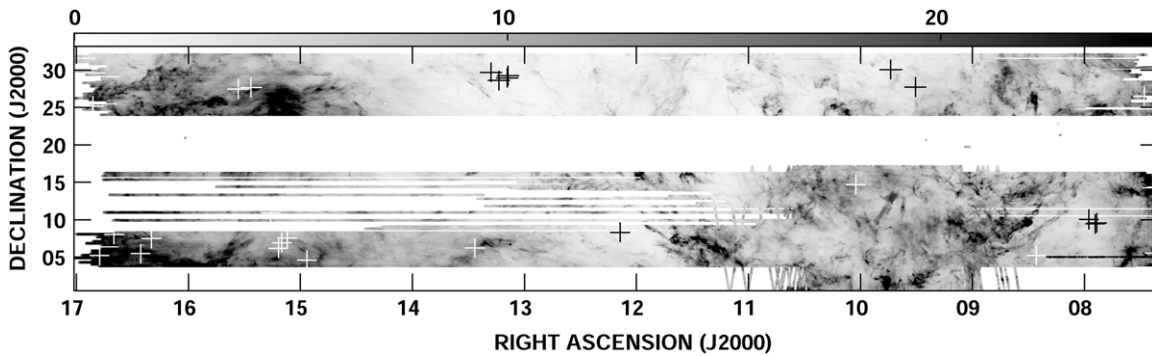
Figure 1. Peak brightness temperature image made using GALFA-H I data for the "Spring" portion of the survey. The velocity range used for making the map is $-120 < V_{LSR} < 120$ km s^{-1}. The gray-scale units are Kelvin. The crosses show the location of detected compact clouds. The size of the crosses has been scaled by a factor of ~30 for visual clarity. The color of the crosses is chosen to get a good contrast with the background gray scale.

allows us to probe a new regime of faint, small H I objects that have not been seen before in lower resolution surveys, e.g., the Leiden/Argentine/Bonn (LAB) survey and the Galactic All Sky Survey (GASS; Kalberla et al. 2005; McClure-Griffiths et al. 2009) or lower sensitivity surveys, e.g., Canadian Galactic Plane Survey (CGPS) (Stil et al. 2006b). In particular, in this paper we focus on a population of strikingly compact and isolated H I clouds detected primarily at Galactic velocities.

The structure of this paper is organized in the following way. Section 2 summarizes the GALFA-H I observations and data reduction. In Section 3, we describe our search for compact H I clouds and provide a catalog of basic cloud properties. The cloud properties, their distribution models, and distance constraints are described in Sections 4–8, while Section 9 discusses various possible origins of this cloud population.

2. OBSERVATIONS AND DATA PROCESSING

The GALFA-H I survey consists of many individual projects, being observed in both solo modes and commensally with the Arecibo Legacy Fast ALFA Survey (ALFALFA; Giovanelli et al. 2005), Arecibo Galaxy Environment Survey (AGES; Auld et al. 2006), and the Galactic ALFA Continuum Transit Survey (GALFACTS; Guram & Taylor 2009) as the Turn-On GALFA Spectrometer (TOGS) and TOGS2 projects. Data cubes used for this study have been made by the core GALFA-H I group[7] and are based on the first data release (released separately as "Spring" and "Fall" data cubes), which uses data from TOGS and several smaller, targeted GALFA-H I projects. The Spring data cubes contain 1030 hr of Arecibo observing time and cover over ~2550 deg^2 including the projects TOGS and a2220 (PI: J. Peek). The Fall data cubes contain 830 hr over ~2050 deg^2 comprising the projects TOGS, a2050 (PI: Peek & Heiles) and a2172 (PI: C. Heiles). The observing method used is drift scanning for TOGS and basketweave scanning for the other projects. The details of the observing modes are summarized in Stanimirović et al. (2006) and Peek & Heiles (2008).

To generate the H I data cubes, raw data obtained with the Arecibo L-band Feed Array (ALFA) were reduced using the GALFA-H I standard reduction pipeline, the details of which are described in Peek & Heiles (2008). The typical rms noise is in the range of 75–120 mK (per 0.736 km s^{-1} velocity channels), depending on the area covered under different GALFA-H I projects. The data used in this study have not been corrected

for the first sidelobe. From our analysis, we find that this effect is small and does not have a significant impact on our results. For example, the first-sidelobe correction leads to an increase in the peak brightness temperature of <10%–15%, a decrease in the velocity line width by ~5%, and a decrease in the cloud size by ~10%–15%.

Figures 1 and 2 show the sky coverage of the GALFA-H I data used in this study for the "Spring" and "Fall" portion of the survey. There are still significant gaps in the survey coverage, resulting in a non-uniform sampling of the right ascension–declination (R.A.–decl.) space. In terms of Galactic coordinates, the current survey coverage consists of three main areas: $l = 0°$–$60°$ and $b \sim 30°$–$60°$, $l = 60°$–$180°$ and $b \sim -50°$ to $-20°$, and $l = 200°$–$250°$ and $b \sim 20°$–$50°$. The total angular search area used for our compact cloud study is ~4600 deg^2, though on the completion of the GALFA-H I survey an area of 13000 deg^2 will be available for an expanded search.

3. COMPACT H I CLOUDS

3.1. Search Method

The standard survey data cubes were combined to produce two sets of larger cubes which are easier for visual inspection, viz., (1) low velocity resolution data cubes of size $40° \times 18° \times 1500$ km s^{-1} with a velocity resolution of 7.4 km s^{-1}, and (2) high velocity resolution data cubes of $40° \times 18° \times 240$ km s^{-1} with a velocity resolution of 1.8 km s^{-1}. Each three-dimensional (R.A.–decl.–velocity) data cube was visually inspected using the visualization program KVIS (part of KARMA; Gooch 1996). The data cubes were searched for *compact* and *isolated* clouds. The clouds which appeared to be a part of some larger, filamentary structure were not considered.

The first round of the visual search was performed using the low velocity resolution data cubes over a wide velocity range of $-750.0 < V_{LSR} < 750.0$ km s^{-1}. The compact clouds of interest were mainly found within the velocity range of $-120.0 < V_{LSR} < 120.0$ km s^{-1}. Compact clouds found outside this range were relatively rare and were generally identified as known galaxies. Therefore, in this paper we focus only on the clouds with $-120.0 < V_{LSR} < 120.0$ km s^{-1}.

The second round of the search was performed using the high-resolution data cubes, restricting the search velocity range to $-120.0 < V_{LSR} < 120.0$ km s^{-1}. Each selected cloud was then inspected in the original high velocity resolution (0.18 km s^{-1}) data cube to reject any spurious or very faint signals and also to measure individual cloud properties. In total, 96 clouds were

---

[7] http://sites.google.com/site/galfahi/Home
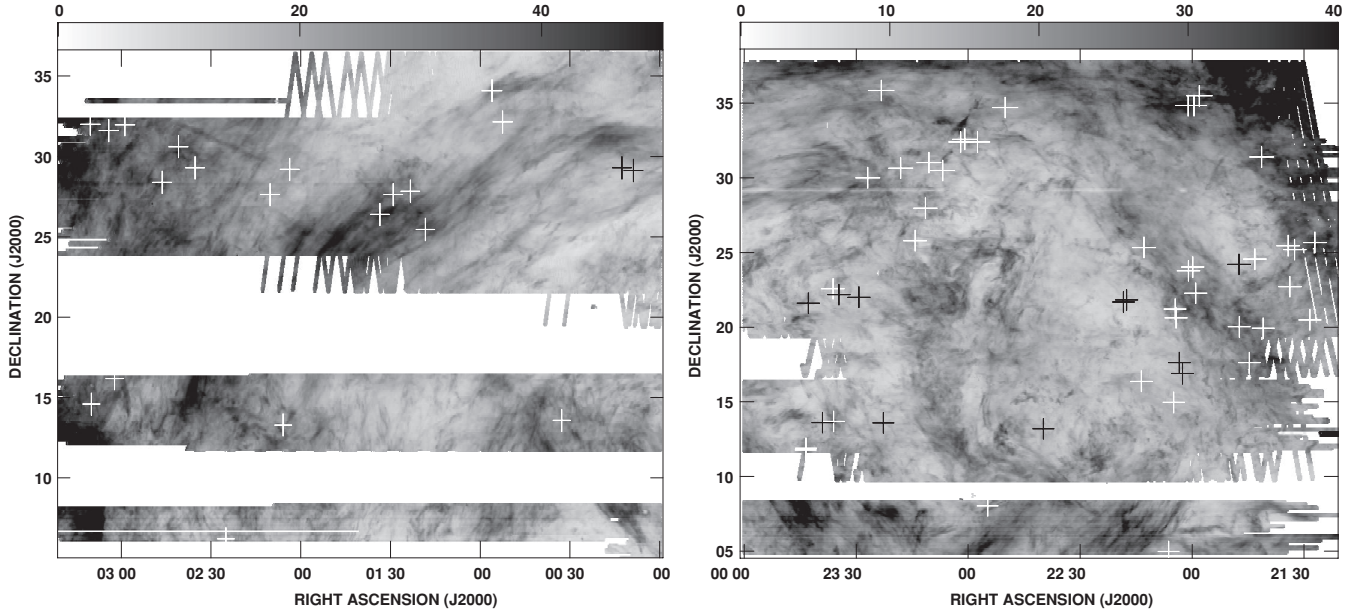
Figure 2. Peak brightness temperature map made using GALFA-H I data for the "Fall" portion of the survey. The velocity range used for making the map is $-120 < V_{\rm LSR} < 120$ km s^{-1}. The gray-scale units are Kelvin. The crosses show the location of detected compact clouds. The size of the crosses has been scaled by a factor of $\sim$16 for visual clarity. The color of the crosses is chosen to get a good contrast with the background gray scale.

identified. The cloud properties are presented and discussed in the following sections.

3.2. Cloud Catalog

We have compiled a catalog of 96 compact H I clouds in Table 1. Column 1 is the cloud catalog number; Columns 2 and 3 are R.A. and decl. in J2000; Columns 4 and 5 are the Galactic longitude (l) and latitude (b); Column 6 gives the size in arcminutes, estimated as the geometrical mean of the measured angular extent along the major and minor axes ($\theta = \sqrt{\theta_{\max} \times \theta_{\min}}$); Columns 7 and 8 give the central LSR velocity ($V_{\rm LSR}$, measured in km s^{-1}) of the fitted Gaussian components (only one value is given if the velocity profile can be well fit with a single Gaussian function); Columns 9 and 10 give the velocity FWHM line width(s) of the fitted Gaussian components, ΔV, in km s^{-1}, Columns 11 and 12 are the peak brightness temperature(s) of the fitted Gaussian components, $T_b^{\rm pk}$, in Kelvin; and Column 13 is the H I column density, $N_{\rm H I}$, measured in units of 10^{18} atoms cm^{-2}. $N_{\rm H I}$ is derived under the assumption that the gas is optically thin.

Cloud size was determined using the total integrated H I column density maps, by fitting an ellipse to the half-peak $N_{\rm H I}$ contour, after background subtraction. No correction was applied to the angular size for the convolution with the Arecibo main beam and sidelobes. The integrated velocity profile for each cloud was obtained by averaging over the area of the cloud. For each profile, the background level was determined by fitting a polynomial function (typically a second or third order, depending on the baseline shape) to the line-free channels around the integrated line profile of the cloud. The baseline-subtracted velocity profile for each cloud was then fitted with one or two Gaussian functions.

The positions of all clouds, overlaid on the peak brightness temperature image for both the Spring and Fall portions of the survey, are shown in Figures 1 and 2. An example peak brightness temperature image at a velocity of -53 km s^{-1}, showing two compact H I clouds, is presented in Figure 3.
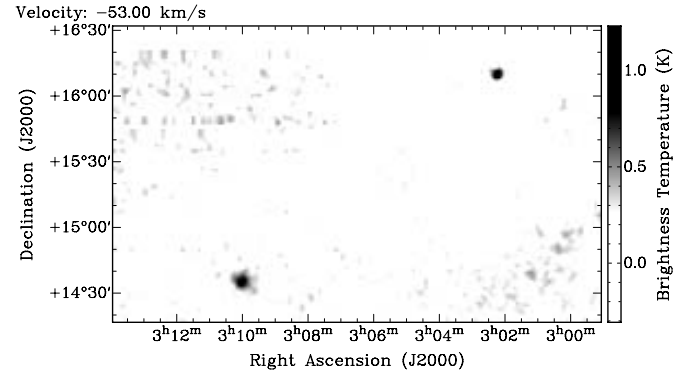
Figure 3. GALFA-H I image at $V_{\rm LSR} = -53$ km s^{-1}, showing two example compact H I clouds, nos. 18 (upper right) and 20 (lower left).

Several examples of H I velocity profiles at the cloud center, with estimated baselines and fitted Gaussian functions, are shown in Figure 4.

3.3. Completeness Test

In order to check the completeness of our cloud catalog, we injected fake compact clouds in several of the large survey data cubes ($40° \times 18° \times 240$ km s^{-1} size). The fake clouds were injected at random locations with input parameters, viz., LSR velocities, FWHM, amplitudes, angular sizes, aspect ratios, and position angles, chosen randomly from a range determined by the observed cloud properties. Further, as suggested by observations, both the velocity profile and the spatial distribution of each fake cloud were modeled with Gaussian functions. Four different simulations were tried, each sampling a different range of FWHM and peak brightness temperature of the compact clouds.

1. *Simulation A.* Bright clouds with a narrow velocity line width: $T_b^{\rm pk} = 1.2$–3.2 K, FWHM = 2.0–6.0 km s^{-1}.
2. *Simulation B.* Bright clouds with a wide velocity line width: $T_b^{\rm pk} = 1.2$–3.2 K, FWHM = 6.0–12.0 km s^{-1}.

Table 1
The Compact Cloud Sample with Derived Gaussian Parameters

Cloud No.	R.A. (J2000) (h:m:s)	Decl. (J2000) (d:m:s)	l (deg)	b (deg)	θ (′)	$v_{\rm LSR}^1$ (km s^{-1})	$v_{\rm LSR}^2$ (km s^{-1})	ΔV^1 (km s^{-1})	ΔV^2 (km s^{-1})	$T_b^{\rm Pk_1}$ (K)	$T_b^{\rm Pk_2}$ (K)	$N_{\rm H\,I}$ (10^{18} cm^{-2})
1	00:08:46	29:07:30	111.83	−32.82	4.97	25.84	...	4.20	...	0.19	...	1.19
2	00:12:38	29:17:30	112.86	−32.82	7.12	−38.41	...	3.66	...	0.61	...	3.97
3	00:32:46	13:34:30	116.00	−49.04	3.74	47.21	...	17.59	...	0.32	...	8.26
4	00:52:30	32:08:30	123.19	−30.72	6.93	−49.98	−50.53	0.42	2.97	0.08	0.16	1.00
5	00:56:06	34:05:30	124.03	−28.77	3.5	50.09	...	4.84	...	0.79	...	6.30
6	01:18:21	25:27:30	130.54	−37.01	5.12	−50.60	−47.50	1.98	17.79	0.28	0.29	11.29
7	01:23:22	27:50:30	131.50	−34.49	9.80	31.30	...	5.39	...	0.69	...	6.92
8	01:29:06	27:37:30	133.06	−34.50	5.61	−56.14	...	5.62	...	0.63	...	5.22
9	01:33:34	26:23:30	134.53	−35.52	3.50	28.79	...	4.46	...	0.39	...	2.59
10	02:03:42	29:11:30	141.35	−32.08	5.59	47.60	...	4.64	...	0.34	...	2.79
11	02:05:54	13:17:30	149.35	−45.72	4.47	27.76	...	2.71	...	0.28	...	1.18
12	02:10:14	27:37:30	143.56	−32.06	3.50	−52.08	−51.95	3.98	13.20	0.36	0.25	9.24
13	02:25:02	06:12:30	160.55	−49.70	5.59	−43.90	...	12.02	...	0.39	...	6.31
14	02:35:21	29:17:30	148.65	−28.33	6.75	−38.79	...	3.29	...	0.65	...	3.69
15	02:40:54	30:36:30	149.19	−26.62	3.50	57.57	...	7.54	...	0.37	...	3.78
16	02:46:22	28:23:30	151.55	−28.01	5.48	44.11	...	3.60	...	0.63	...	4.11
17	02:58:46	31:58:30	152.15	−23.57	4.0	−60.02	...	2.00	...	0.60	...	2.11
18	03:02:14	16:10:30	163.01	−36.31	3.50	−51.91	−50.38	3.37	11.87	0.39	0.25	8.32
19	03:04:10	31:36:30	153.42	−23.28	5.86	−53.07	−52.38	1.86	5.51	1.74	0.19	8.21
20	03:10:02	14:35:30	166.06	−36.41	3.50	−53.46	...	10.27	...	0.34	...	4.87
21	03:10:22	32:00:30	154.39	−22.24	9.95	−48.07	−51.98	6.36	16.50	0.19	0.36	13.99
22	07:28:10	26:30:30	192.32	19.30	6.71	−84.46	−80.11	4.23	18.65	0.34	0.22	10.62
23	07:53:30	29:34:30	211.25	18.09	5.48	−31.81	...	6.87	...	0.19	...	1.72
24	07:54:22	09:26:30	211.48	18.23	3.60	−29.68	...	6.12	...	0.15	...	1.22
25	07:57:37	10:02:30	211.27	19.21	3.74	−31.00	...	0.85	...	0.48	...	0.77
26	08:25:54	05:13:30	219.23	23.36	7.35	55.36	...	4.81	...	0.11	...	0.81
27	09:30:38	27:42:30	200.06	45.75	3.97	−120.64	...	3.71	...	0.21	...	1.33
28	09:43:50	30:02:30	197.38	48.99	3.86	−111.14	...	1.06	...	0.15	...	0.23
29	10:02:29	14:43:20	221.70	48.86	6.12	−43.76	...	4.22	...	1.08	...	7.77
30	12:08:46	08:18:30	272.73	68.64	4.62	61.76	...	13.26	...	0.59	...	9.78
31	13:08:46	29:14:30	62.90	85.63	5.74	−30.11	...	1.75	...	0.35	...	1.19
32	13:09:18	28:56:30	58.67	85.66	4.00	−28.91	...	2.39	...	0.49	...	1.72
33	13:13:42	28:35:30	50.78	84.86	3.86	−26.28	−28.05	1.73	5.59	0.31	0.11	2.26
34	13:17:54	29:40:30	58.11	83.64	5.41	−24.45	−31.00	5.63	12.63	0.53	0.35	14.53
35	13:26:38	06:13:30	326.32	67.48	8.46	14.27	19.92	4.60	10.52	0.07	0.17	4.21
36	14:56:34	04:35:30	1.43	52.62	6.00	−74.43	...	13.83	...	0.25	...	4.81
37	15:07:06	07:32:30	7.89	52.38	4.40	−27.67	...	5.10	...	0.27	...	1.99
38	15:10:06	06:56:30	7.81	51.42	4.99	−80.48	...	14.77	...	0.27	...	5.05
39	15:11:50	06:11:30	7.24	50.63	5.92	−18.66	−19.93	2.61	6.60	0.81	0.16	6.19
40	15:15:54	10:56:30	14.51	52.41	4.74	34.98	...	6.73	...	0.44	...	4.23
41	15:26:30	27:39:30	42.97	55.72	6.71	−52.19	−66.99	8.66	15.82	0.08	0.44	14.94
42	15:33:18	27:26:30	43.00	54.19	6.48	−26.83	...	3.13	...	0.35	...	1.78
43	16:19:46	07:29:30	21.24	36.99	4.11	−47.19	−37.62	6.68	10.88	0.11	0.35	8.94
44	16:25:38	05:28:30	19.93	34.74	3.62	−30.15	−36.95	5.17	6.31	0.27	0.19	5.06
45	16:39:50	08:02:30	24.66	32.85	6.20	−17.80	−20.23	3.37	8.97	0.68	0.26	8.89
46	16:47:38	05:13:30	22.80	29.82	5.87	53.01	...	14.86	...	0.53	...	11.34
47	16:51:10	25:10:30	45.20	36.69	7.48	−34.79	−42.44	6.08	13.83	0.49	0.29	13.83
48	21:27:06	25:40:30	75.48	−17.83	5.48	27.76	...	2.02	...	0.43	...	1.66
49	21:28:26	20:29:30	71.66	−21.58	7.48	37.45	...	5.11	...	0.86	...	7.44
50	21:32:30	25:11:30	76.00	−19.05	4.74	24.53	...	1.64	...	1.55	...	4.24
51	21:33:46	22:42:30	74.31	−20.98	6.71	29.11	...	3.35	...	1.86	...	10.49
52	21:34:14	25:27:30	76.49	−19.14	5.37	15.35	...	2.80	...	1.69	...	8.81
53	21:40:58	19:55:30	73.39	−24.11	5.49	22.01	23.19	0.60	4.26	0.51	0.82	7.37
54	21:41:22	31:23:30	82.02	−15.99	5.84	−39.49	−35.38	2.48	4.94	0.32	0.73	8.63
55	21:43:10	24:33:30	77.34	−21.21	4.97	32.89	...	6.34	...	1.23	...	11.39
56	21:44:42	17:37:30	72.23	−26.34	4.90	23.35	...	5.98	...	1.05	...	10.28
57	21:47:22	20:01:30	74.62	−25.12	3.50	32.62	...	2.61	...	0.61	−	2.65
58	21:47:26	24:12:30	77.83	−22.14	5.74	78.05	...	8.04	...	0.74	...	9.17
57	21:58:02	35:29:30	87.53	−15.19	7.00	19.27	...	3.42	...	1.31	...	7.18
60	21:59:02	22:16:30	78.52	−25.37	6.06	71.41	...	6.57	...	0.75	...	6.51
61	21:59:30	34:50:30	87.35	−15.89	6.11	29.98	25.03	3.74	3.99	1.05	0.71	13.22
62	21:59:50	24:01:30	79.96	−24.19	4.24	23.11	...	2.72	...	1.38	...	6.91
63	22:00:58	23:46:30	79.99	−24.55	5.46	22.91	...	3.26	...	1.23	...	6.79
64	22:01:06	34:50:30	87.61	−16.09	6.48	24.79	...	3.71	...	1.17	...	7.71

Table 1
Continued

Cloud No	R.A. (J2000) (h:m:s)	Decl. (J2000) (d:m:s)	l (deg)	b (deg)	θ (′)	v^1_{LSR} (km s^{-1})	v^2_{LSR} (km s^{-1})	ΔV^1 (km s^{-1})	ΔV^2 (km s^{-1})	$T^{Pk_1}_b$ (K)	$T^{Pk_2}_b$ (K)	$N_{\mathrm{H\,I}}$ (10^{18} cm^{-2})
65	22:02:34	16:53:30	75.06	−29.88	6.48	21.98	...	4.50	...	0.95	...	7.52
66	22:03:26	17:37:30	75.82	−29.48	5.24	49.37	...	7.20	...	1.09	...	11.43
67	22:04:18	20:37:30	78.30	−27.41	5.20	33.11	...	6.36	...	0.92	...	8.92
68	22:04:34	21:12:30	78.79	−27.02	6.34	39.01	37.39	3.77	8.82	1.58	0.39	18.43
69	22:04:54	14:57:30	73.98	−31.66	4.12	58.52	...	5.62	...	0.31	...	2.67
70	22:06:18	04:58:30	65.41	−38.80	7.65	−47.42	−46.84	2.62	12.50	0.48	0.38	11.77
71	22:13:34	16:22:30	76.91	−32.04	5.11	54.28	...	4.23	...	0.91	...	6.67
72	22:17:34	21:49:30	81.84	−28.51	6.24	−30.72	...	2.36	...	1.13	...	4.86
73	22:18:22	21:41:30	81.91	−28.73	5.24	−34.72	...	2.39	...	1.19	...	4.82
74	22:12:54	25:20:30	83.38	−25.10	5.74	−69.86	−71.43	4.17	18.09	0.41	0.37	16.46
75	22:39:50	13:11:30	80.36	−38.56	5.24	−32.76	...	2.19	...	0.83	...	3.34
76	22:50:06	34:42:30	96.36	−21.82	8.66	12.66	13.72	1.84	3.59	2.50	0.51	12.56
77	23:11:26	27:58:30	97.42	−29.89	3.50	75.52	...	4.49	...	0.59	...	3.10
78	23:14:14	25:47:30	96.98	−32.13	4.74	42.57	...	2.01	...	0.97	...	3.74
79	23:22:42	13:35:30	92.28	−43.93	3.74	−63.10	−62.16	1.93	3.89	0.22	0.15	1.99
80	23:26:54	30:00:30	101.93	−29.39	4.97	−37.63	−35.95	1.99	2.87	0.63	0.21	3.99
81	22:54:46	08:02:30	80.00	−44.88	4.08	−60.13	...	9.22	...	0.44	...	5.41
82	22:57:30	32:24:30	96.65	−24.58	5.74	16.19	18.39	2.20	4.91	1.41	0.23	8.21
83	23:00:54	32:35:30	97.44	−24.75	7.12	15.39	...	1.88	...	4.13	...	15.14
84	23:01:58	32:24:30	97.57	−25.01	5.74	18.12	18.24	1.87	3.28	4.45	1.21	23.96
85	23:06:50	30:29:30	97.65	−27.19	4.50	39.95	40.17	2.39	12.86	0.71	0.46	14.77
86	23:10:30	31:01:30	98.71	−27.05	8.0	−24.01	...	1.91	...	1.26	...	4.56
87	23:18:06	30:39:30	100.21	−28.06	6.48	24.58	24.28	2.61	7.16	1.02	0.51	12.26
88	23:23:18	35:51:30	103.54	−23.67	6.87	−53.14	...	4.33	...	2.61	...	20.74
89	23:29:14	22:00:30	98.88	−36.99	5.59	8.97	...	1.45	...	1.64	...	3.81
90	23:34:38	22:10:30	100.41	−37.31	6.15	−21.74	...	3.74	...	1.44	...	8.49
91	23:36:02	13:41:30	96.44	−45.26	4.74	−64.30	...	1.93	...	1.23	−	4.66
92	23:36:14	22:34:30	101.43	−37.07	5.98	13.90	...	1.91	...	2.40	...	8.52
93	23:39:02	13:36:30	97.34	−45.63	6.71	−54.89	−56.07	2.18	5.43	2.22	0.24	11.98
94	23:42:50	21:36:30	102.42	−38.51	7.35	10.61	...	2.53	...	3.02	...	13.59
95	23:43:26	11:53:30	97.80	−47.63	4.00	−47.34	...	2.54	...	0.83	...	3.51
96	23:43:30	11:46:30	97.76	−47.74	5.00	−52.54	...	3.03	...	2.45	...	13.64

3. *Simulation C.* Faint clouds with a narrow velocity line width: $T^{pk}_b = 0.2$–1.2 K, FWHM = 2–6 km s^{-1}.

4. *Simulation D.* Faint clouds with a wide velocity line width: $T^{pk}_b = 0.2$–1.2 K, FWHM = 6–12 km s^{-1}.

The range of V_{LSR} over which clouds were injected was kept the same for all four simulations, as $-120 \leqslant V_{LSR} \leqslant +120$ km s^{-1}. Similarly, the cloud angular size, position angle, and aspect ratio were in the range 3.0–8.0 arcmin, 0°–180°, and 1.0–2.0, respectively. For each simulation, 15 fake clouds were injected. The input parameters of the injected clouds were noted to be later compared with the list of recovered clouds.

The data cube with injected fake clouds was then searched by eye following the same criteria adopted for the selection of "real" compact cloud as discussed in Section 3.1. The list of detected compact clouds was compared with the list of injected fake clouds to compute the fraction of fake clouds missed by our search. Table 2 summarizes the results of our completeness test. Column 1 shows the simulation type, and Column 2 the detection rate for the fake clouds. Column 3 shows the fraction of fake clouds with $V_{LSR} \sim 0$ km s^{-1}; compact clouds with $V_{LSR} \sim 0$ km s^{-1} were missed in the search because of confusion with bright Galactic emission. Column 4 shows the fraction of fake clouds which appeared to be spatially connected to some large-scale emission. Column 5 shows the fraction of detected real clouds in our catalog, with properties similar to the input parameters of the simulations.

Table 2
Results of Fake Clouds Simulations

Simulation	Detection Rate	Confusion	Connected	Observations
Case A	13/15	0	2/15	22/96
Case B	10/15	3/15	2/15	0/96
Case C	8/15	0	2/15	52/96
Case D	9/15	2/15	1/15	22/96

As fake clouds were injected at random locations in the data cubes, with V_{LSR} selected randomly in the specified range of −120 to 120 km s^{-1}, some of the fake clouds have $V_{LSR} \sim 0$ km s^{-1}. Such clouds were missed by our search as velocity channels around $V_{LSR} \sim 0$ km s^{-1} are dominated by bright Galactic emission. Quantitatively, we find that we cannot recover any fake clouds placed in regions where the Galactic background (as determined from the LAB survey; Kalberla et al. 2005) exceeds 4 K, but that in regions below 4 K our recovery rate does not substantially depend on the Galactic background emission. This is consistent with our finding that few real clouds were detected with V_{LSR} close to 0 km s^{-1} (see Figure 5). In addition, some of the fake clouds were missed as they coincided spatially with large-scale structures, hence they were rejected by our selection criteria. Taking into consideration the above two cases, we find a detection rate of 100% for the clouds which are bright and have either narrow or wide velocity line widths. However, when the clouds are faint, their detection rate
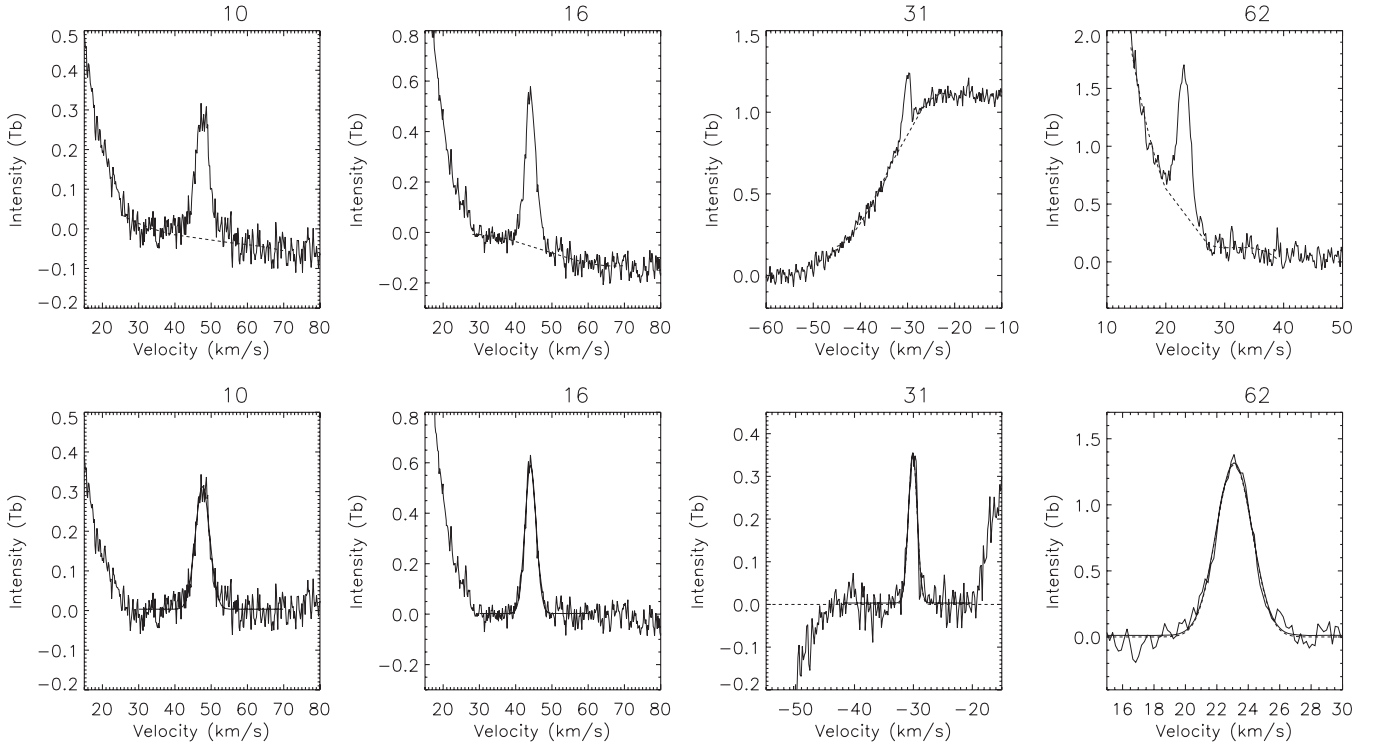
Figure 4. Four examples of H I velocity profiles of compact H I clouds. The dashed line in the top panels shows the estimated baseline, while the solid line in the bottom panels represents Gaussian functions fitted to the H I line profile.

decreases to 80% in the case of narrow velocity line widths, and 70% in the case of broad velocity line widths.

Comparing the fake cloud detection rate with the real cloud detections suggests that (1) a lack of bright compact clouds with wide velocity line widths in our catalog is a real feature and not a selection effect, (2) it is unlikely that we have missed any bright clouds with narrow velocity widths in the regions where Galactic background does not exceed 4 K, and (3) the observed decrease in the number of detections of faint compact clouds with a wide line width is likely to be a selection bias. To summarize, in our selected region of study ($\sim$4600 deg^2), we cannot recover any compact clouds in regions where the Galactic background exceeds 4 K. On the other hand, in regions with Galactic background below 4 K, we are most likely missing about one quarter of the clouds, in total, due to our selection biases.

4. OBSERVED CLOUD PROPERTIES

4.1. Clouds Size, Peak Brightness Temperature, and Central Velocity

Figure 5 shows histograms of basic observed properties for the whole compact cloud sample: angular size, peak LSR velocity, $V_{\rm LSR}$, and peak brightness temperature, $T_b^{\rm pk}$.

The clouds are typically very compact, with the median angular size of the sample being $\sim$5'. Many clouds are unresolved at Arecibo's resolution, at least in one dimension. A large fraction of the sample has an unresolved core along with some faint diffuse emission, as seen in Figure 3. The extent of this faint diffuse emission is most likely slightly overestimated (by about an arcmin) due to the telescope sidelobes.

The majority of clouds have $T_b^{\rm pk} = 0.5$–2 K, while the median peak brightness temperature for the whole sample is 0.75 K. This low peak brightness temperature, coupled with the small

angular size, explains why such clouds were largely missed by previous large-scale Galactic H I surveys, e.g., the GASS and LAB surveys (McClure-Griffiths et al. 2009; Kalberla et al. 2005).

Clouds are found at both positive and negative LSR velocities. The $V_{\rm LSR}$ histogram has a nearly symmetric distribution around $V_{\rm LSR} = 0$ km s^{-1}. A lack of clouds between $-20 \leqslant V_{\rm LSR} \leqslant 5$ km s^{-1} is not real, but due to difficulties in finding clouds in the presence of bright Galactic emission, as discussed in Section 3.3. It is interesting to note that if we neglect bins $|V_{\rm LSR}| < 20$ km s^{-1}, a Gaussian function could be fit with a peak at $\sim$0 km s^{-1} and a standard deviation of $\sim$42 km s^{-1}.

As observed clouds have typically $|b| \sim 30°$–$50°$ (see Table 1), Figure 6 shows the l versus $V_{\rm LSR}$ plots of the LAB survey integrated over $30° < b < 50°$ (left) and $-50° < b < -30°$ (right), with the positions of compact clouds with $b > 0°$ and $b < 0°$ overplotted, respectively. Most clouds are found in the first and second Galactic quadrants, at least partially due to our limited survey coverage, and appear at velocities both allowed and forbidden by Galactic rotation. To quantify the extent to which cloud velocities deviate from the velocity expected from Galactic rotation, we define the deviation velocity (Wakker 1991) as

$$V_{\rm dev} = \begin{cases} V_{\rm LSR} - V_{\rm min}(l, b) & \text{if} \quad V_{\rm LSR} < 0 \\ V_{\rm LSR} - V_{\rm max}(l, b) & \text{if} \quad V_{\rm LSR} > 0, \end{cases} \quad (1)$$

where ($V_{\rm min}, V_{\rm max}$) is the range of velocities allowed by Galactic rotation for a given (l, b) direction. For clouds following Galactic rotation, $V_{\rm dev} = 0$. Considering that the above definition of $V_{\rm dev}$ does not account for the velocity dispersion due to random and turbulent motions, clouds with $|V_{\rm dev}| < 20$–30 km s^{-1} are often considered as not being at forbidden velocities. Traditionally, high-velocity clouds (HVCs) are assumed to have $|V_{\rm dev}| > 60$ km s^{-1} and $|V_{\rm LSR}| > 90.0$ km s^{-1}, while
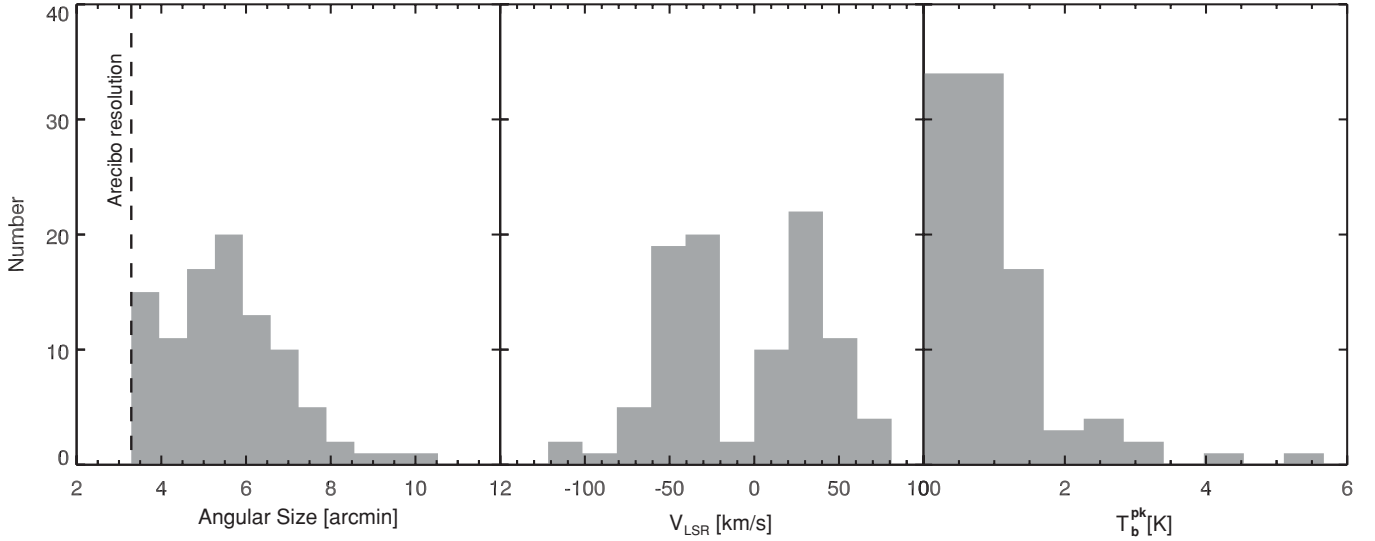
Figure 5. Histograms of basic observed properties for the whole sample of compact clouds: angular size, peak V_{LSR}, and the peak brightness temperature, T_b^{pk}.
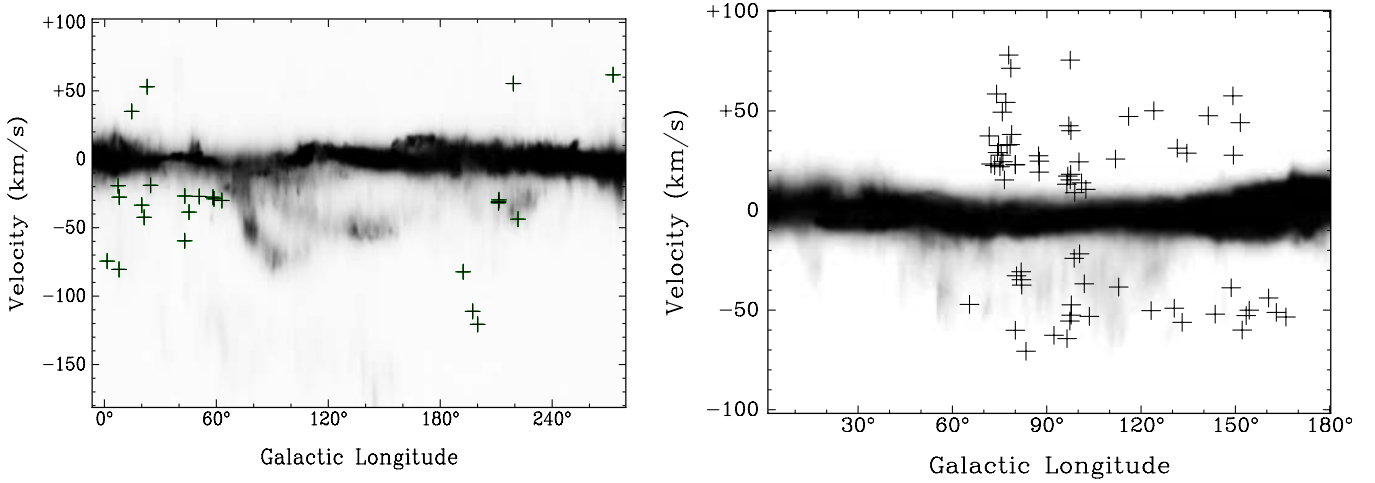
**Figure 6.** Left: position–velocity diagram for the Milky Way centered at $b = 40°$ and integrated over the range $b = [30°:50°]$, using data from the LAB survey. The positions of compact clouds with $|b| > 0°$ are plotted as crosses. Right: position–velocity diagram for the Milky Way centered at $b = -40°$ and integrated over the range $b = [-50°:-30°]$, using data from the LAB survey. The positions of compact clouds with $|b| < 0°$ are plotted as crosses.

intermediate velocity clouds (IVCs) have $|V_{LSR}| = 40$–$90\,\mathrm{km\,s^{-1}}$ (Wakker 2004).

We find that $\sim 33\%$ (32/96) of the sample clouds have $V_{dev} \sim 0.0$, i.e., velocities allowed by Galactic rotation. For the remaining clouds with non-zero V_{dev}, most of the clouds deviate from Galactic rotation by $|V_{dev}| \leqslant 50\,\mathrm{km\,s^{-1}}$ (with a majority showing $V_{dev} \sim 20\,\mathrm{km\,s^{-1}}$). Figure 7 shows the histogram of deviation velocities for the whole catalog; clouds with $V_{dev} \sim 0\,\mathrm{km\,s^{-1}}$ have not been included in this graph. We find that only two clouds in our sample (cloud nos. 27 and 28) have $|V_{dev}| > 60\,\mathrm{km\,s^{-1}}$ and $V_{LSR} > 90.0\,\mathrm{km\,s^{-1}}$, hence can be classified as HVCs. Similarly, only a few compact clouds can be classified as IVCs.

4.2. Clouds FWHM, $N_{H\,I}$, and $T_{K,max}$

Figure 8 shows histograms of the velocity FWHM (ΔV), the H I column density ($N_{H\,I}$), and the upper limit on the kinetic temperature (i.e., the kinetic temperature in the case of no non-thermal broadening, defined as $T_{K,max} = 21.86\Delta V^2$). As discussed in the next sub-section, some clouds have multi-Gaussian velocity profiles, and for such clouds we include
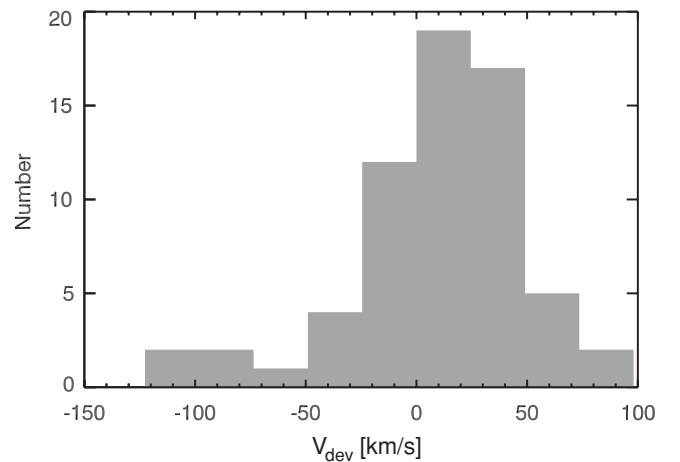
Figure 7. Histogram of the deviation velocity for the compact clouds population. Only clouds with non-zero V_{dev} have been included in the plot.

only the brightest component when considering the above quantities.
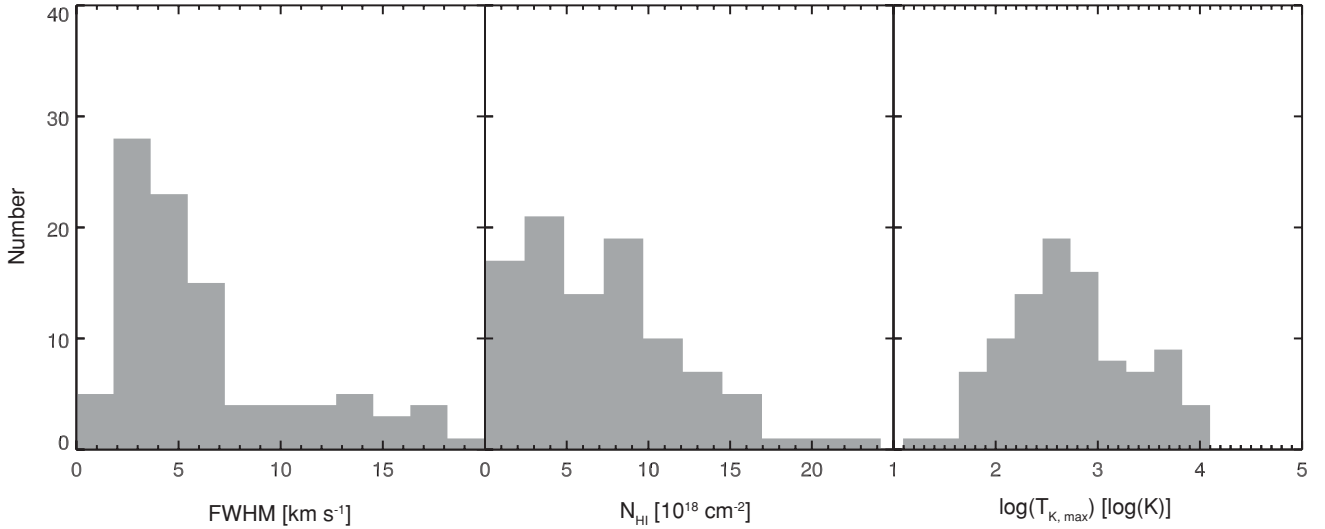
Figure 8. Histograms showing distributions of FWHM, $N_{\rm H\,I}$ and log(kinetic temperature) for the compact cloud sample.

Generally, the FWHM for the sample is in the range of $\sim$1–8 km s^{-1}, with a median FWHM of 4.2 km s^{-1}. Most of the clouds are cold (in cases where the velocity profiles were fitted with a single Gaussian) or have a cold core (in the case of double Gaussian fits). The median $T_{K,\max}$ of the sample is only 300 K. In their H I absorption survey, Heiles & Troland (2003b) found the CNM spin temperature of 50–70 K (for $|b| > 10°$) and a typical sonic Mach number of about 3. This results in a typical CNM kinetic temperature $T_{k,\max} \sim$ 150–250 K. Our median $T_{k,\max} = 300$ K is very similar to what is found for the CNM clouds seen in absorption, suggesting that these compact clouds have properties similar to those of typical Galactic CNM clouds.

The integrated H I column density distribution peaks at 5×10^{18} cm^{-2}, with $\sim$80% of clouds having $N_{\rm H\,I} < 10^{19}$ cm^{-2}. This is low relative to typical Galactic CNM clouds which typically have $N_{\rm H\,I} > 10^{19}$ cm^{-2}. Our H I column density was derived assuming the gas to be optically thin, an assumption that is reasonable because the emission is faint. As many compact clouds are unresolved or only marginally resolved with the Arecibo, the beam dilution effect is likely to be important for the smallest clouds, and hence the derived $N_{\rm H\,I}$ could be lower than the true $N_{\rm H\,I}$. For example, high-resolution interferometric follow-up observations (J. E. G. Peek et al. 2010, in preparation) of some of the compact clouds unresolved with Arecibo revealed bright compact cores (sizes below the resolution of 28 arcsec) embedded in a diffuse emission, with a peak $N_{\rm H\,I} \sim 10$ times the value seen by Arecibo.

In Figure 9, we compare our compact clouds with typical Galactic CNM and WNM clouds, and also with interstellar clouds found in the local ISM (LISM). The corresponding H I column density and $V_{\rm LSR}$ of LISM clouds were compiled by Muller et al. (2006) and originate from H I, D^0, and Ca$^+$ observations toward stars within 50 pc. The same quantities are also plotted for the CNM and WNM Galactic clouds from the Heiles & Troland (2003a) survey, for high latitude lines of sight ($|b| \geqslant 25°$). LISM clouds (shown with crosses) have a distribution symmetric about $V_{\rm LSR} \sim 0$ km s^{-1}, and $N_{\rm H\,I} \sim 2 \times 10^{18}$ cm^{-2}. This is significantly lower than what is measured for the CNM/WNM, $N_{\rm H\,I} >$ a few $\times 10^{19}$ cm^{-2} (shown with circles). The H I column density of our compact clouds (shown with triangles), even after taking into account the
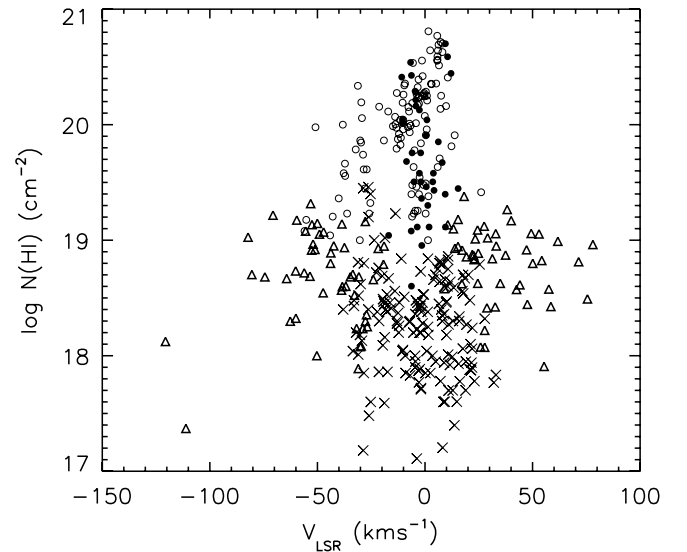

Figure 9. Velocity distribution of compact clouds (shown as triangles) along with LISM clouds (shown as crosses). The LISM clouds are toward stars within 50 pc (Muller et al. 2006); the data for LISM clouds are taken from Frisch et al. (2002), Redfield & Linsky (2002), and Wood et al. (2005). Also shown in the plots are the CNM (solid circles) and WNM (empty circles) Galactic clouds are from Heiles & Troland (2003a). Only sight lines with $|b| \geqslant 25°$ are considered.

beam dilution effect, fills in the gap between LISM clouds and the CNM/WNM clouds. The velocity distribution of compact clouds is however more extended than that of the other two populations. The gap in the distribution of compact clouds around $V_{\rm LSR} \sim 0$ km s^{-1} is not real, but due to the presence of strong Galactic emission.

Another population of Galactic CNM clouds with similarly low H I column density was discovered recently by Braun & Kanekar (2005) and Stanimirović & Heiles (2005) through H I absorption measurements. These so-called low-column-density absorbers have a peak optical depth of 10^{-2}, an FWHM of 3 km s^{-1}, and a typical H I column density $N_{\rm H\,I} \sim 6 \times 10^{18}$ cm^{-2} (Stanimirović et al. 2007). In fact, Braun & Kanekar (2005) observed several compact H I blobs in H I emission near one such absorber, with angular sizes of only $\sim$2–3 arcmin.
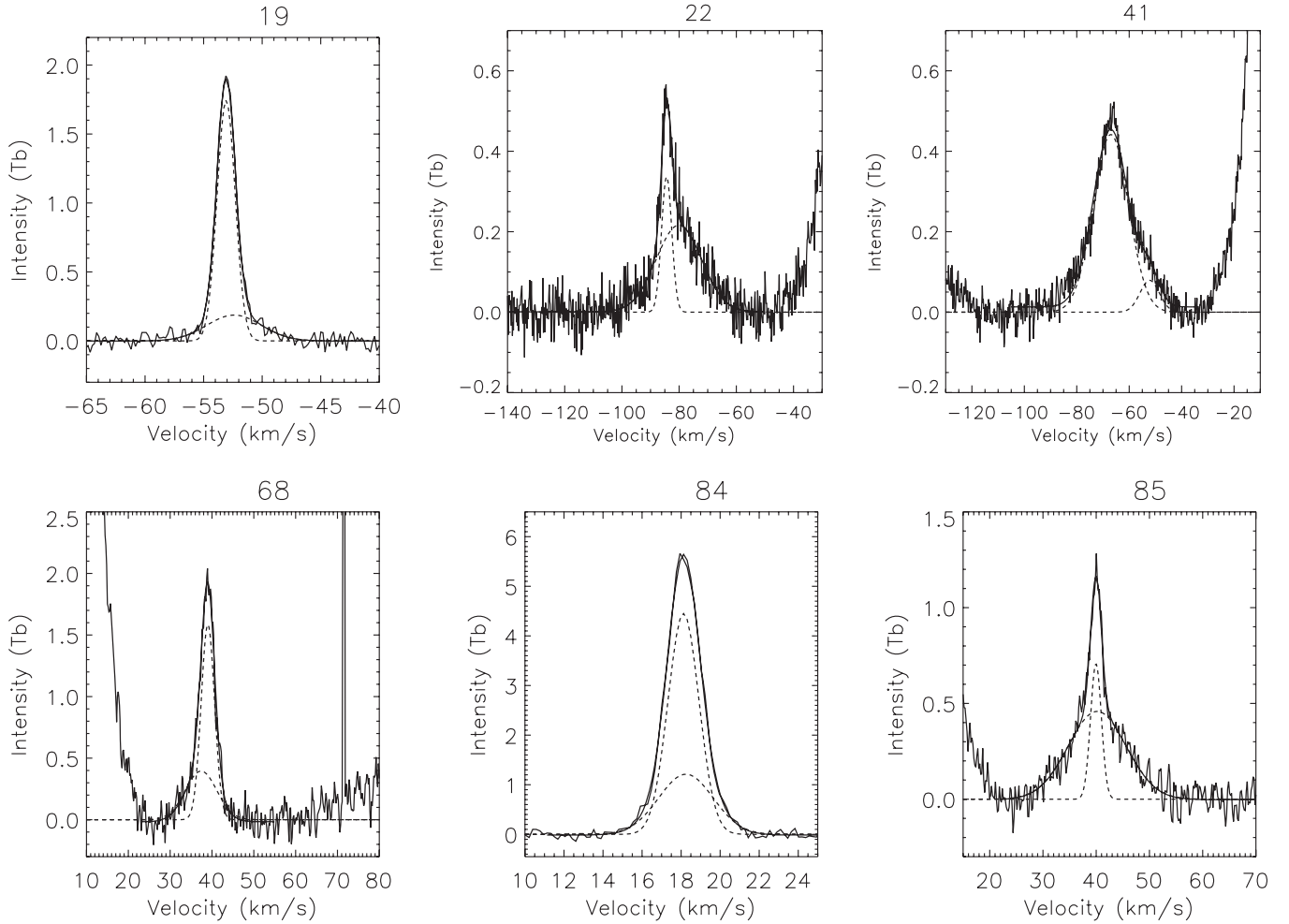
Figure 10. Several examples of H I line profiles fitted with two Gaussian functions. Two Gaussian components are shown with dashed lines.

4.3. H I Line Profile Shapes: Evidence for a Multiphase Medium

For each compact cloud, the integrated H I line profile was first fitted with a single Gaussian component and the residuals were inspected. H I profiles in some cases were found to deviate significantly from a simple Gaussian function. Such profiles were then fitted with a greater number of Gaussian components. We found that in 66/96 (∼69%) cases a single Gaussian function provided a good representation to the line profiles, whereas in 30/96 (31%) two Gaussian functions were required to fit the observed profiles. Examples of some shapes of line profiles fitted with a double Gaussian component are provided in Figure 10.

For some clouds with double Gaussian components (e.g., clouds nos. 84 and 85 in Figure 10), velocity profiles show evidence for a core-halo structure with two spectral components. A narrow and bright Gaussian function is required to fit the line center, while a faint and broad component is needed to fit the line wings. Such cases could indicate the existence of a multiphase medium. However, in most cases with double Gaussian fits (17 out of 30 clouds), line profiles show weak, broad velocity tails, e.g., $V_{LSR} \sim [-80, -60]$ km s^{-1} for cloud no. 22 in Figure 10. In such cases, the narrow Gaussian component is significantly offset in velocity from the broad Gaussian component. Such profiles with weak velocity tails are likely to be due to the contribution of diffuse Galactic background emission, and/or superposition of different clouds along the line of sight (LOS).

Hence, for computing the physical parameters for clouds with multiple Gaussian fits, only the brighter Gaussian component was considered for the rest of the analysis.

In order to characterize motions of the colder cores (represented by narrow Gaussian functions) relative to the warmer envelopes (represented by broad Gaussians) for those clouds with velocity profiles well fit by two Gaussian functions, we estimated the sonic Mach number (**M**) of the cores. Following Kalberla & Haud (2006), we define **M** as the ratio of the absolute difference between the centers of the two fitted Gaussian functions to the FWHM of the broader function:

$$\mathbf{M} = \frac{|V_{\text{Wide}} - V_{\text{Narrow}}|}{\text{FWHM}_{\text{Wide}}}. \quad (2)$$

The **M** histogram in Figure 11 shows a peak at **M** = 0.1 and a tail all the way to **M** = 1.5. About half of the multiphase clouds have **M** $\lesssim$ 0.2 and 2/3 of the multiphase sample has **M** $\lesssim$ 0.4. Clouds with **M** $\gtrsim$ 0.2 show velocity tails. Clouds with **M** $\lesssim$ 0.2, which are likely to have real multiphase signatures, have cold cores with low Mach numbers, indicating that the cold cores are moving subsonically within warmer envelopes. For comparison, Heiles & Troland (2003b) found supersonic internal motions for Galactic CNM clouds with **M** $\sim$ 3, while Kalberla & Haud (2006) found that most HVCs have **M** $\sim$ 1.5 for cold cores relative to their warm envelopes. This may suggest that compact clouds are less turbulent than Galactic CNM clouds
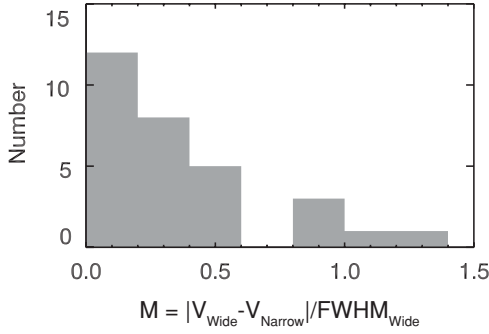
Figure 11. Histogram showing the ratio of the absolute difference between the centers of the two fitted Gaussian functions to the FWHM of the broader function, for the clouds whose velocity profiles are represented by two Gaussian functions.

or HVCs. However, we are most likely underestimating **M** due to our inability to spatially resolve cold cores.

4.4. Compact Clouds with Velocity Gradients

The high spatial and velocity resolution of the GALFA-H I survey allows us to investigate velocity gradients across H I clouds. We find that 31 clouds in our sample (i.e., 32% of the clouds) show velocity gradients. To map the velocity gradient, we derived the velocity centroid at each position in the cloud, using the intensity-weighted first moment map. Before obtaining the moment map, LOSs with a low signal-to-noise ratio were excluded by applying a cutoff at the 2σ level, σ being the rms noise level in a line-free channel. This was done after the smoothing of data cubes in velocity (using boxcar smoothing three channels wide) and position (using a Gaussian with FWHM $\sim$ 1.5 times that of the Arecibo beam). Further, for compact clouds with velocities close to Galactic emission, each velocity channel was inspected and pixels with Galactic emission were blanked before obtaining the velocity field.

Figure 12 shows two example velocity fields, while Figure 13 shows the histogram of measured velocity gradients, along the kinematic major axis. We typically find a velocity gradient of $\sim$0.5–1 km s^{-1} arcmin^{-1}. However, since the clouds are mainly unresolved, the observed velocity gradient could be significantly affected by beam smearing; beam smearing leads to an increase in the size of the cloud and a decrease in the observed velocity gradient. Our measured velocity gradient is therefore most likely underestimated.
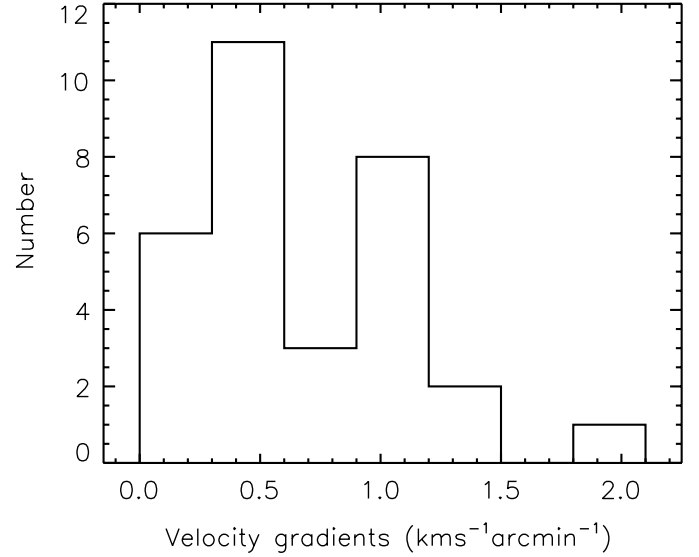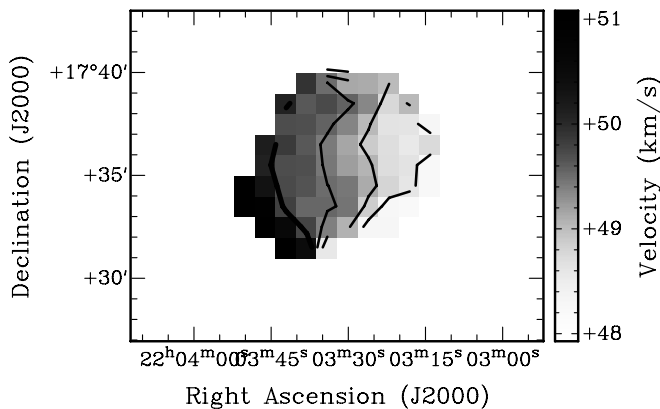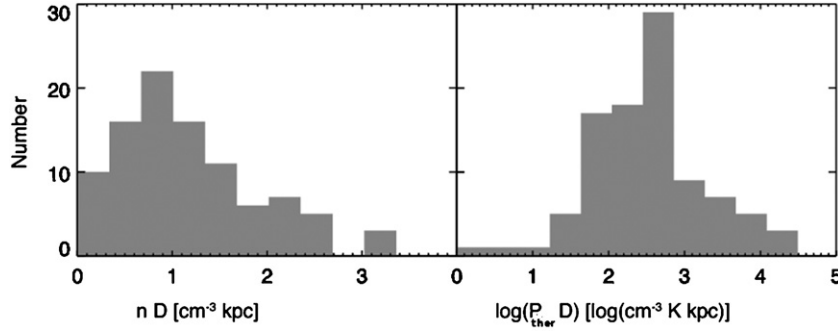

Figure 13. Histogram of the velocity gradient per unit angular size for the 31 compact clouds with a velocity gradient.

One possibility is that the velocity gradients arise due to fluctuations in the background H I emission, especially for the clouds in regions with complicated Galactic emission. We note, however, that all of the clouds with systematic gradients are found to be very isolated with no strong background Galactic emission. Further, for each cloud with a velocity gradient, the line profiles were carefully inspected to check for baseline stability. No systematic change in the baseline shape was found. These tests suggest that the measured velocity gradients are inherent to the clouds.

A large-scale velocity gradient could be a signature of rotation in the case of self-gravitating clouds. For example, velocity gradients have been noted in many CO studies of molecular clouds in the Milky Way and in M33 (Philips 1999; Rosolowsky et al. 2003). As we discuss in the next section, our clouds are very far away from being gravitationally bound. Velocity gradients have also been observed in H I clouds associated with circumstellar H I in the direction of evolved stars (Gerard & Le Bertre 2006), and have been explained in terms of expansion in the H I shell due to stellar mass loss. In this case, the observed clouds (or filaments) are likely to be inclined along the LOS and the observed velocity gradient is most likely
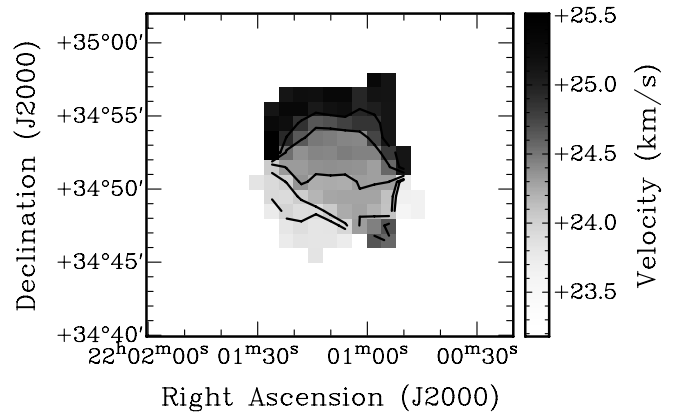
Figure 12. H I velocity field for two compact clouds with significant velocity gradient. Left: cloud 66—the contours are in steps of 0.5 km s^{-1}, starting from 48.5 km s^{-1}. Right: cloud 64—the contours are in steps of 0.3 km s^{-1}, starting from 23.7 km s^{-1}.

Figure 14. Histograms showing the H I volume density and log(thermal pressure) distributions for the compact clouds.

underestimated. If a cloud/filament is inclined at an angle ϕ with respect to our LOS, and $\phi = 0°$ then no velocity gradient would be observed as all parts of the filament would lie along the LOS. Similarly, if $\phi = 90°$, velocities would be perpendicular to the LOS and hence no gradients observed. For any other value of ϕ, the observed velocity gradient will on average be less than the intrinsic velocity gradient. This, together with the beam smearing effect, suggests that our measured average velocity gradient of ~ 0.5–1.0 km s^{-1} arcmin^{-1} is likely to be underestimated and a more reasonable value may be ~ 2 km s^{-1} arcmin^{-1}.

For comparison, the velocity gradient seen in low-mass dwarf galaxies is typically greater than 2 km s^{-1} arcmin^{-1} (Begum et al. 2008, 2006). High-resolution interferometric follow-up observations of compact clouds are clearly needed, and are already underway, to provide detailed maps of the clouds velocity fields.

5. DERIVED CLOUD PROPERTIES

We can use the measured cloud properties to derive the H I volume density, the thermal pressure, and the H I mass for the compact cloud population. Assuming compact clouds to be spherical, the volume density is $n \propto N_{\rm H I}/(D \times \theta)$ and the thermal pressure is $P_{\rm ther} \propto n T_{K,\rm max}$, with D being the unknown cloud distance. We note that, as $T_{K,\rm max}$ is derived from the observed FWHM, which can have a contribution from turbulent motions, the estimated $P_{\rm ther}$ represents only an upper limit on thermal pressure. Also, for unresolved clouds the measured angular size θ is only a lower limit on the cloud size. Both n and $P_{\rm ther}$ depend on the cloud distance D. As cloud distances are unknown, we show in Figure 14 quantities (nD) and $\log(P_{\rm ther}D)$. To obtain true n and $P_{\rm ther}$ values, the derived quantities should be divided by the distance (measured in kpc). At a distance of 1 kpc, for example, $n \sim 1$ cm^{-3} and $P_{\rm ther} \sim 300$ K cm^{-3}. We explore this concept further in later sections.

We can now test the hypothesis that clouds are gravitationally bound. The virial mass, $M_{\rm vir}$, is given as $M_{\rm vir} = 190\Delta V^2 r$, where r is the cloud size in pc, ΔV is the velocity FWHM in km s^{-1}, and $M_{\rm vir}$ is in units of solar mass. Figure 15 (right) shows the histogram of $M_{\rm vir} \times D^{-1}$ for the whole cloud sample. The median $M_{\rm vir} \times D^{-1}$ for the sample is $2 \times 10^3 M_\odot$ kpc^{-1}, whereas the median H I mass for the sample is ~ 0.1 $M_\odot$ kpc^{-2} (see Figure 15, left). This implies that $\frac{M_{\rm vir}}{M_{\rm H I}} \sim \frac{2 \times 10^4}{D(\rm kpc)}$. Hence, for $D \sim$ a few kpc, gravity is totally negligible, unless a large amount of dark matter is invoked to stabilize the clouds.

6. COMPARISON WITH OTHER SURVEYS

6.1. HVC and IVCs

In order to find an association, if any, between the compact clouds and well-known HVCs and IVCs, the compact cloud sample was cross-correlated with the catalog of HVCs and IVCs by Wakker (2001). We find that a subset of clouds, viz., clouds nos. 48–57 with $l \sim 75°$ and $b \sim -20°$, lie close to a region having a large number of scattered, faint IVCs. This field is a part of Complex GP HVC (Figure 18 in Wakker 2001), having a distance limit of 0.8 kpc $< D <$ 4.3 kpc. However, there is a ~ 30 km s^{-1} difference between the lowest velocity found for the GP complex and the first cloud we detect in this region. Hence, an association of these compact clouds with the Complex GP HVC is not very likely.

Similarly, several compact clouds around $l \sim 155°$ and $b \sim -30°$ (clouds nos. 13–21) lie close to the Cohen Stream and HVC WW507 (Figure 9 in Wakker 2001). The limit on the distance to the Cohen Stream and WW507 is > 0.3 kpc. Again, as in the case of Complex GP, there is a ~ 25.0 km s^{-1} difference between the lowest velocity gas associated with this complex and our clouds detected in this region. We therefore conclude that an association between compact clouds and cataloged HVC and IVC complexes is unlikely.

6.2. Comparison with Na I and Ca II Absorption Lines

The compact cloud sample was cross-correlated with the recent catalog of Na I and Ca II absorption measurements toward 1857 early-type stars located within 800 pc of the Sun (Welsh et al. 2010). Na I and Ca II absorption relatively close to our clouds would allow us to place a constraint on the cloud distance. Only one possible correlation was found within our search radius of ~ 7 arcmin. In this case, cloud no. 46 is located at an angular separation of only ~ 1.7 arcmin from HD 151525 (at a distance of 141 pc). However, the $V_{\rm LSR}$ of the Na I/Ca II absorption is significantly different from that of the cloud H I emission, suggesting that the cloud is likely to be at $D \geqslant 141$ pc.

6.3. Variable Stars

Braun & Kanekar (2005) and Dedes et al. (2008) suggested possible shell-like structures associated with several small H I clouds. As this points to a potential mass-loss cloud origin, we correlated our cloud catalog with the catalog of variable stars (Downes et al. 2006[8]). The catalog includes novas, nova-like variables, Mira variables, interacting binary dwarfs, etc. For

---

[8] http://archive.stsci.edu/prepds/cvcat/
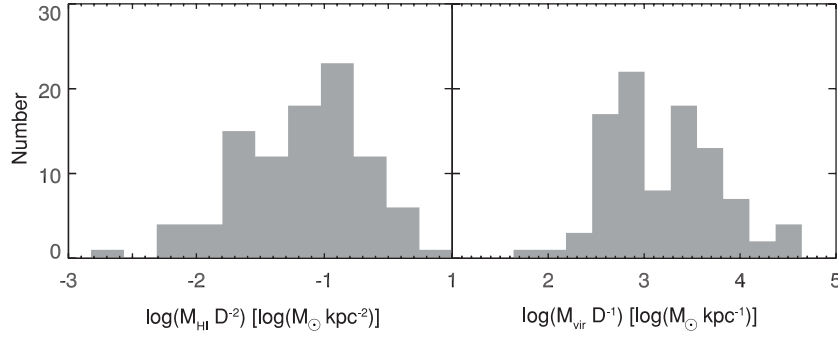
Figure 15. Histograms showing the distributions of H I mass and virial mass for the compact clouds.

one of the compact clouds (cloud no. 31), a "nova-like" variable star (Com) was found within 10 arcmin of the clouds, and for 12 clouds (i.e., 12.5% of the sample of clouds), there is a variable star within $1°$. If, on the other hand, we randomly select 96 LOSs, we find that $\sim$7.0% of those LOSs have at least one variable star within a degree. This suggests that a potential correlation between variable stars and compact clouds may be more than a chance alignment.

6.4. Optical/UV/IR Extragalactic Surveys

For each detected compact cloud, the NASA Extragalactic Database (NED) was searched at the location of the cloud center for possible optical/UV/IR counterparts. The search was performed within 3.5 arcmin of the peak of the cloud H I distribution. No diffuse optical/UV emission was detected at cloud positions in the DSS, Sloan Digital Sky Survey (SDSS), or *Galaxy Evolution Explorer* (*GALEX*) imaging surveys. For 39 compact clouds (i.e., 40% of the sample of clouds), an extended IR source was found within a search radius of 3.5 arcmin in the Two Micron All Sky Survey (2MASS) extended source catalog. Nothing is known about the nature of these IR sources; no optical redshifts are known for any of the sources, hence their association with the H I clouds is yet to be confirmed. However, this potential correlation with the IR sources is more likely to be a chance alignment, as for 96 randomly selected LOSs, $\sim$43% have at least one 2MASS extended source within 3.5 arcmin.

7. DISTANCE CONSTRAINTS: CLOUD DISTRIBUTION MODELS

In this section, we compare the distributions of compact clouds in Galactic latitude (b), Galactic longitude (l), and radial velocity (V_{LSR}) to models of cloud populations in order to constrain physical characteristics of the population, such as distances and intrinsic velocities.

7.1. Galactic Latitude Distribution

By examining the distribution in Galactic latitude of the detected clouds, we can determine whether they are linked to the Galactic disk: a distribution that is oblate in the plane of the Galaxy would indicate a relationship to the Galactic disk. The method is to construct a simplified model of the distribution of these clouds and then compare it with our observed distribution using the Kolmogorov–Smirnoff (K-S) D-statistic. The D-statistic is simply the largest difference between the cumulative distribution functions (CDFs) of the data and model. In this way, we can fit a parameter in our simplified model to the data.

We choose a model that captures the relative scale distance at which these objects can be seen in the plane of the Galaxy to the scale height of a population above the disk. We call this ratio of scales R. If the clouds are independent of the orientation of the Galactic plane, the K-S D-statistic should be at a minimum for a spherical distribution, $R = 1$. If they do follow the plane, and can be seen out past their Galactic scale height, $R > 1$ should have a significantly smaller D-statistic. Our model simply assumes that clouds are equally detectable along the surface defined by

$$L^2 = x^2 + y^2 + (Rz)^2, \qquad (3)$$

where L is an arbitrary distance, x, y, and z are distances from the Sun, with x toward the Galactic center and z pointing toward the north Galactic cap. We also assume the probability of detecting a cloud at great distance drops to zero, and that the functional form by which it drops is the same along each axis. We then compute the distribution of clouds we expect to observe from this model as a function of R, given the footprint of the GALFA-H I data set, and compute the K-S D-statistic.

As shown in Figure 16, we find that a spherical distribution is a much poorer fit to the data ($D_{R=1} = 0.276$) than an oblate distribution ($D_{R=10} = 0.129$), but that we cannot distinguish between distributions with $R \geqslant 10$. This is because we have very little coverage in the Galactic plane, where a very oblate distribution would generate a very large number of clouds. Therefore, we see evidence that significantly more clouds are located toward the plane of the disk. This suggests an oblate cloud distribution and implies that the bulk of the clouds are related to the disk.

As mentioned in Section 2, the Arecibo telescope does not allow an unbiased access to all Galactic latitudes. Currently, most of our coverage is at intermediate Galactic latitudes, $|b| \sim 20°$–$50°$. We will add in the future data from lower latitudes: $b = [-10{:}10]$ from Inner-Galaxy ALFA Low-Latitude H I Survey (I-GALFA). This will allow us to better constrain the latitude modeling and/or any potential variation in the cloud properties with Galactic latitude.

7.2. Galactic Velocity Distribution

We extend the analysis of the previous section by examining the distribution of velocities. In theory, it is possible to use the distribution of velocities to determine whether the clouds are corotating with the disk or whether they are independent of disk rotation. This velocity distribution, interesting in its own right, can also help shed light on the typical distances to the clouds. In addition, modeling of the velocity distribution depends less on our incomplete survey coverage (Section 2) and offers a wider range of data points for the comparison of various distributions.
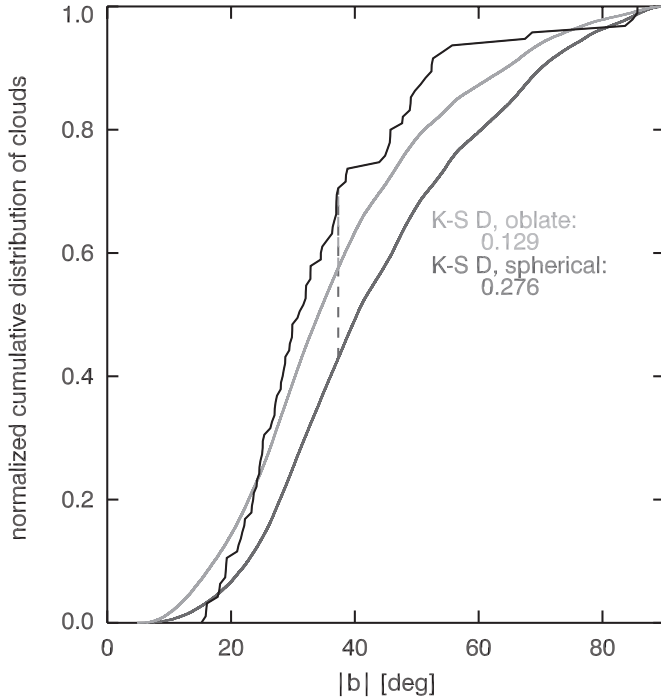
Figure 16. Normalized cumulative distribution of sample clouds plotted as a function of Galactic latitude. The same quantity is plotted for the two models with Galactic clouds having spherical and oblate distributions. The dashed line shows where the D-statistic is computed, i.e., where the difference between the model and the observed cumulative distribution function is the largest.

7.2.1. Galactic Model

In this model, we generate a large number of clouds which populate (l, b, v) space, and have velocities related to the bulk rotation of the Galactic disk. To do this, we assume the clouds populate an oblate distribution with $R = 10$ and some variable distance scale L (see Equation (3)). We assume the clouds follow cylindrical Galactic rotation with a flat rotation curve at $\Theta_0 = 220$ km s^{-1}. In addition to their rotation velocity, we impart to them a variable random radial velocity, σ. We constrain the clouds to lie in our observational footprint and to meet the simple detection criterion that they do not lie in regions with background brightness temperature in H i above 4 K, which is consistent with our completeness test (Section 3.3). We compute this background brightness using the 36' resolution LAB survey (Kalberla et al. 2005).

We find that comparing our model to the data does not constrain the distance to the clouds under the assumption of corotation. We can, however, fit to the random velocity component, σ, independent of L and corotation. Using the K–S D-statistic, as in Section 7.1, we find that a random radial velocity of 45 km s^{-1} is near the best fit to the data, with a variation from this value of 10 km s^{-1} being noticeably worse (see Figure 17). Assuming there is no preferential direction for this random velocity, we can multiply by $\sqrt{3}$ to find a true 3-space random velocity of $\sigma_3 \sim 80$ km s^{-1}.

7.2.2. Circumgalactic Model

We can also generate a model with the basic assumption that the clouds are beyond, but around, the Galaxy, and therefore have v_{GSR} velocities near to zero (i.e., they are in the rest frame of the Milky Way's barycenter). As in the Galactic model, we include the selection effects of our data set when producing the model. We include a σ of 45 km s^{-1} as in the Galactic model.
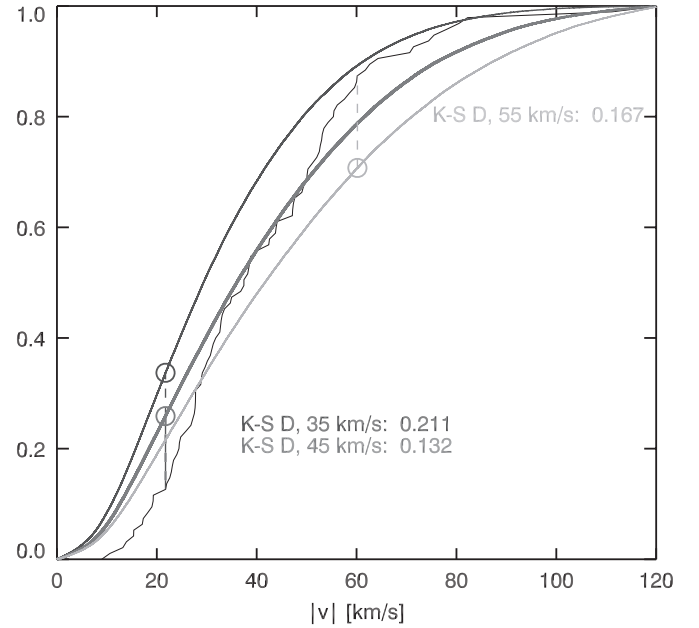

Figure 17. Normalized cumulative distribution of sample clouds plotted as a function of Galactic LSR velocity. Smooth lines show modeled cumulative distributions for a varying random velocity component. The dashed line shows where the D-statistic is computed, i.e., where the difference between the model and the observed cumulative distribution function is the largest.

We find that the circumgalactic model is qualitatively a very poor fit to the data (see Figure 18)—many observed clouds lie in areas where the model predicts almost no clouds (e.g., $V_{LSR} \simeq 30$ km s^{-1}, $l \simeq 90°$), and the model predicts many clouds where none are observed (e.g., $V_{LSR} \simeq -90$ km s^{-1}, $l \simeq 150$ km s^{-1}). We note that by increasing σ we could modify the model to predict more clouds in areas where there are discrepancies, but this would have the effect of also producing more model clouds out to extreme velocities, where clouds are not observed. Based on this model, we conclude that the observed clouds must be related to the Galactic disk. This conclusion is consistent with, but entirely independent of, our conclusion in Section 7.1.

8. DISTANCE CONSTRAINTS: OTHER METHODS

The distances to some of the cataloged clouds in the first and fourth Galactic quadrants can be measured using the tangent-point method. The LSR velocity at tangent points (V_t), positions where the LOS is perpendicular to a circle of constant Galactocentric radius, was measured from ^{12}CO observations by Clemens (1985). We find that 17 clouds in the first Galactic quadrant have $V_{LSR} - V_t < 30$ km s^{-1}. If we assume that all these clouds are at the tangent point but their velocities have been perturbed from V_t by random motions (Stil et al. 2006a; Ford et al. 2008), we can then estimate the clouds' tangent-point distance: $d_t = R_\odot \cos l / \cos b$ (with $R_\odot = 8.5$ kpc being the Galactocentric radius of the solar circle). Under the further assumption that Galactic rotation is constant with distance from the plane, we find that d_t ranges from 0.4 to 3 kpc, with a median distance being 2.2 kpc. This would result in a median height from the Galactic Plane $h_z = d_t \times \sin b \sim 1$ kpc.

Another distance constraint comes from the method applied by Stanimirović et al. (2006). Compact clouds are cold with properties similar to what is found for typical Galactic CNM clouds, or they show evidence for the existence of cold cores surrounded by warm envelopes. To explain the coexistence of
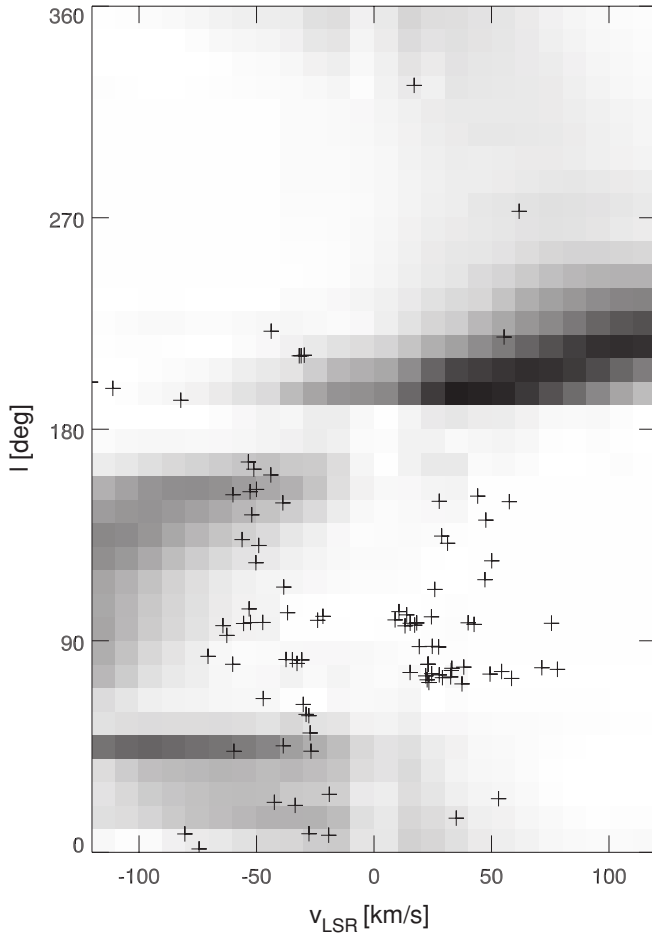
Figure 18. Galactic longitude as a function of V_{LSR}. The crosses show the sample compact clouds, whereas the gray scale represents the circumgalactic model of the compact clouds (see the text for more details).

the CNM and WNM, heating and cooling conditions need to be considered locally (Wolfire et al. 2003), and a well-defined range of thermal pressures is needed. For example, at $R_g = 8.5$ kpc, $P_{min} \sim 2000$, and $P_{max} \sim 5000$ K cm^{-3}. We can compare this pressure requirement with our pressure histogram in Figure 14. For a thermal pressure typical for the solar neighborhood of 3000 K cm^{-3}, a distance of ~ 100 pc is required. Wolfire et al. (2003) showed that the lowest thermal pressure allowed for the CNM and WNM to coexist is ~ 300 K cm^{-3}. This would place an upper limit on the cloud distance of ~ 1–3 kpc. This is in agreement with the tangent-point method and suggests a possible distance range of 0.1–3 kpc.

The cloud V_{LSR} distribution in Figure 5, roughly symmetric with a similar number of clouds having either negative or positive V_{LSR}, places another constraint on the cloud distance. As most clouds in the sample have $|b| > 30°$, a cloud distance > 3 kpc would imply a height above the Galactic plane that is >1 kpc. At such heights, Galactic rotation is lower than in the midplane of the Galaxy (Marinacci et al. 2010; Kalberla & Kerp 2009; Levine et al. 2008; Collins et al. 2002). This results in the V_{LSR} distribution for the whole sample to be skewed toward negative velocities. This effect of a lag in clouds rotation velocity at high $|z|$ resulting in the LSR distribution getting skewed toward negative LSR velocities has been noted for the HVCs' distribution (Peek et al. 2009) and the Milky halo stars (Schneider 2006). As we do not observe this effect when

considering the whole sample of compact clouds suggests that a majority of clouds are likely to be at a distance $\leqslant 3$ kpc.

9. DISCUSSION

Based on the modeling of spatial and velocity distributions of the whole compact cloud population, we have shown that the bulk of the compact clouds are related to the Galactic disk. The tangent-point method and the consideration of the conditions required for the CNM/WNM coexistence in the ISM suggest that cloud distances are likely to be in the range of 0.1 to a few kpc. However, this still does not exclude the possibility for a few clouds to be located at very large distances. As possible scenarios for the cloud origin depend on distance, we discuss several possibilities in the following subsections.

9.1. Galactic Compact Clouds at Sub-parsec Scales

For a distance $\leqslant 1$ kpc, with a typical size of $\leqslant 1$ pc, we are dealing with nearby Galactic clouds. In this case, a significant fraction of clouds would have $n \geqslant 1$ cm^{-3} and a total pressure ~ 1000 K cm^{-3}. The cloud H I mass (shown in Figure 15, left) would be $< 10^{-1}$ $M_\odot$. However, at a distance as low as 100 pc these properties become slightly more extreme: $n \sim 10$ cm^{-3}, $P_{ther} \sim 3000$ K cm^{-3}, $M_{H I} \sim 10^{-3}$ $M_\odot$, and clouds would have a linear size of $\leqslant 30,000$ AU. At this distance and assuming a velocity gradient of 2 km s^{-1} arcmin^{-1}, the length doubling timescale for clouds/filaments would be very short, $\sim 1.5 \times 10^4$ yr. Such short lifetimes suggest transient and recently produced objects.

In any case, the properties (size, temperature, H I column density, H I mass) of such sub-parsec clouds may be similar to those of the low-column-density absorbers (Braun & Kanekar 2005; Stanimirović & Heiles 2005). This possible connection is also supported by the Westerbork Synthesis Radio Telescope (WSRT) H I emission observations by Braun & Kanekar (2005), who found several compact clouds in the proximity of one of the low-column-density absorbers seen in H I absorption. In this scenario, the compact clouds may represent large and low-column-density examples of the population of CNM clouds on sub-parsec scales. The most extreme CNM clouds, so-called tiny scale atomic structure (TSAS), reach scales of a few AU, appear overdense and overpressured relative to the traditional CNM, and were once postulated to comprise up to 15% of the CNM (Frail et al. 1994; Heiles 1997). The obvious questions are, how do such small and isolated clouds form and survive in the ISM, and what role do they play within the general ISM?

One possible scenario that can explain the formation and maintenance of compact cold clouds in the ISM is interstellar turbulence. Recently, numerical simulations of the ISM have started to describe cold and warm atomic gas with a numerical resolution and dynamic range approaching realistic physical scales, e.g., Vazquez-Semadeni et al. (2006), de Avillez & Breitschwerdt (2005), and Audit & Hennebelle (2005). The numerical simulations by Audit & Hennebelle (2005) show that a collision of incoming turbulent flows can initiate condensation of the WNM into cold neutral clouds. A collision of incoming WNM streams creates a thermally unstable region of higher density and pressure but lower temperature, which further fragments into small cool structures. The abundance of cold structures, as well as their properties, depends heavily on the properties of the underlying turbulent flows. For example, Audit & Hennebelle (2005) find that a significant fraction of the CNM structures formed in the case of very turbulent flows have

thermal pressures of $\leqslant 10^4$ K cm^{-3}, temperatures $\geqslant 100$ K, and volume density $n \leqslant 100$ cm^{-3}. These CNM structures are thermally stable, long lived ($\sim$Myr) and in the case of stronger turbulence they are more rounded, similar to the compact clouds in our sample.

In a similar approach, Koyama & Inutsuka (2002) showed that a thermally unstable shock-compressed layer, formed from the WNM compression by supernova explosions, can also fragment into small, cold, turbulent condensations as a result of the thermal instability. As the ISM is frequently compressed by supernova explosions, fragmentation of the shock-compressed medium can also be a potential mechanism for the formation of compact clouds.

Another possibility may be provided by stellar outflows. H I emission has been detected in the circumstellar shells of a variety of evolved stars, viz., asymptotic giant branch (AGB) stars, oxygen-rich and carbon-rich stars, semi-regular and Mira variables, and planetary nebulae (Gerard & Le Bertre 2006). For example, Matthews et al. (2008) found an extended tail of H I associated with the AGB star Mira and argued that H I tails are likely to be a common feature of evolved stars undergoing mass loss. Furthermore, H I has also been detected in emission/absorption toward several planetary nebulae (Gussie & Taylor 1995; Rodriguez et al. 2002). Our cross-correlation of the compact cloud catalog with the catalog of variable stars by Downes et al. (2006) suggests that a subset of clouds has at least one variable star within a radius of 1°.

The association of H I clouds with variable stars at angular distances of $\sim$1°–2° has been noticed before. Matthews et al. (2008) found H I emission as far as $\sim$1°.5 away from a Mira variable. Gerard & Le Bertre (2006) also reported evidence that H I emission associated with circumstellar envelopes may be offset from the position of the central star. Assuming that the detected H I clouds are the circumstellar H I associated with variable stars, for a typical distance of 100 pc and an expansion velocity of 5 km s^{-1} seen for circumstellar H I (Gerard & Le Bertre 2006), a degree separation of the H I clouds from the variable star corresponds to an H I mass of $\sim$2 × 10^{-3} $M_\odot$, an H I diameter of 1.7 pc, and a characteristic timescale of 0.34 Myr. All three parameters agree well with the ones found in the H I survey of circumstellar envelopes around evolved stars (Gerard & Le Bertre 2006). Hence, it is likely that some of the compact H I clouds could be related to the outflows from these stars.

Once formed by turbulence and/or stellar outflows and injected into the surrounding medium, these isolated compact clouds of cold, low-column-density H I will be immersed in the warm/hot ambient gas. The obvious question that arises is how are such compact clouds able to survive without being quickly evaporated? From Equation (47) in McKee & Cowie (1977), the mass loss of a compact H I cloud embedded in a hot plasma ($T \sim 10^6$ K) is $\sim$7 × 10^{-2} $M_\odot$ Myr^{-1}, whereas if the clouds are embedded in large warm envelopes ($T \sim 7000$ K), the evaporation mass loss is 10 times smaller. This would imply that the compact clouds may be evaporating on a timescale of $\sim$Myr, due to a combination of conductive heat transfer and/or Kelvin–Helmholtz instabilities from the surrounding warm/hot medium (Stanimirović & Heiles 2005; Dedes & Kalberla 2010).

9.2. Compact Clouds in the Disk–halo Interface Region

If at a distance of a few kpc, the majority of compact clouds would have $P_{\text{ther}} \leqslant 100$ K cm^{-3}, $n \sim 1.0$ cm^{-3}, a height of a few kpc above the disk, and a corresponding H I mass of $\sim$0.01–0.3 $M_\odot$. In this scenario, observed cloud properties are similar to numerous H I clouds found in the Galactic disk–halo interface region.

Recent H I observations have shown that the disk–halo interface of our Galaxy is not smooth, but populated with discrete H I clouds. Observations with the Green Bank telescope (GBT) found discrete H I clouds in the halo of the inner Galaxy (Lockman 2002). Although these clouds, often referred to as "Lockman's clouds," are located $\sim$900 pc below the plane, they appear to be dynamically related to the disk. Further, Stil et al. (2006a) discovered many clouds at forbidden velocities in the inner Galaxy using data from the VLA Galactic Plane Survey (VGPS). Despite their forbidden velocities, those clouds follow the Galactic emission. Similarly, Ford et al. (2008) detected over 400 H I clouds in the lower halo of the inner Galaxy using the GASS, with properties similar to the clouds discovered by Lockman (2002). Stanimirović et al. (2006), using the GALFA-H I precursor observations, found numerous clouds in the disk–halo interface of the outer Galaxy, indicating that this phenomenon is not restricted to the inner Galaxy. Finally, using the interferometric data from the WSRT and the Very Large Array (VLA), Bekhti et al. (2009) studied the H I emission at low, intermediate, and high radial velocities along four random LOSs toward quasars which had previous detections of weak Ca II and Na I absorption features. They found several compact and cold clumps of neutral gas at velocities similar to those of the optical absorption.

Table 3 shows a comparison of the compact clouds from this work with the clouds discovered in the recent Galactic surveys. Based on their physical parameters, $N_{\text{H I}}$, T_b^{pk}, and ΔV, compact clouds from the GALFA-H I survey are the most similar to the low-column-density H I clumps seen in the H I interferometric observations along the sight lines of Ca II and Na I absorbers (Bekhti et al. 2009). However, most differences between various studies stem from the difference in angular resolution and sensitivity of various surveys. For example, higher values of $N_{\text{H I}}$ and T_b^{pk} for the Bekhti et al. (2009) clouds compared to our sample are mainly due to the difference in angular resolution of the Arecibo (3.5 arcmin) and WSRT/VLA observations ($\sim$1.6 arcmin). Larger size and velocity line width of the GASS and GBT clouds samples are largely caused by large telescope beams (15 arcmin and 9 arcmin for the Parkes telescope and the GBT, respectively) and the blending of smaller clouds. The H I clouds in the disk–halo interface region are generally thought to originate from the condensation of hot gas expelled from the disk by superbubbles (Houck & Bregman 1990). Hence, these compact clouds in the disk–halo interface could play an important role in studying the mass circulation between the Milky Way disk and the halo.

An alternative mechanism that may be able to explain the existence of compact clouds in the disk–halo interface region was recently proposed by Heitsch & Putman (2009), and involves recooling of inflowing gas. Simulations show that as warm/ionized clouds approach the Galactic disk, they encounter denser and denser material, which leads to the compression of clouds and causes them to slow down and recool, forming intermediate and low-velocity clouds close to the Galactic disk. The compact clouds in our sample may be able to fit into this framework, thus representing a later stage of the infall process for HVCs. The observed compact clouds may be getting integrated and digested by the disk, and hence provide a smooth buildup of fresh star formation fuel for the Galactic disk. The random radial velocity component of 45 km s^{-1} for the clouds

Table 3
Comparison of GALFA-H I Clouds with the Compact Clouds from Other Galactic Surveys/Studies

Parameters	GALFA-H I (This Work)	GASS (Ford et al. 2008)	VGPS (Stil et al. 2006a)	Lockman Clouds (Lockman 2002)	VLA/WSRT (Bekhti et al. 2009)
$N_{\rm H I}(10^{19})$	0.5	1.4	18.0	2.0	0.9
$T_b^{\rm pk}$ (K)	0.75	0.6	12.3	1.0	1.6
ΔV (km s^{-1})	4.2	12.8	5.6	12.2	4.1
Size (arcmin)	5.0	29.0	3.4	22.3	2.3

found in Section 7.2.1, corresponds to $T_{k,\max} \sim 4.4 \times 10^4$ K, and may be interpreted as compact clouds being condensed out of an extended warm/hot layer in the disk–halo interface as traced by O VI absorption lines (Savage et al. 2003). Future metallicity and dust-to-gas ratio observations of compact clouds would be the crucial test of the cloud infall hypothesis.

9.3. Compact Clouds at Extreme Distances

As discussed in Section 5, if the compact clouds are self-gravitating systems, they have to be extremely dark matter dominated in order to be stable, having more than ∼99% of the total mass as dark. The presence of a large number of such low-mass, dark matter halos have been predicted by cosmological ΛCDM simulations (Klypin et al. 1999; Moore et al. 1999). Sternberg et al. (2002) showed that most of the gas in low-mass halos should be found in a thermally stable, ionized/WNM phase, within which cold cores may be able to form. However, such models require the clouds to be at large distances (⩾100 kpc). We note that although the compact cloud sample as a whole cannot be circumgalactic, from our statistical analysis in Section 7.2, we cannot rule out the possibility that some of the clouds could be at large distances, and hence they could be associated with the dark matter mini-halos in the vicinity of the Milky Way, as predicted by cosmological ΛCDM simulations. Recently, Giovanelli et al. (2010) found a set of isolated, H I sources in the ALFALFA survey and argued that these could be associated with isolated mini-halos in the outskirts of the Local Group. Again, metallicity and dust-to-gas ratio observations of these clouds should be able to address the mini-halo possibility.

10. SUMMARY AND CONCLUSIONS

The GALFA-HH I survey is successfully mapping the entire Arecibo sky at 21 cm. The survey covers a velocity range of -700 to 700 km s^{-1} (LSR) at a velocity resolution of 0.18 km s^{-1} and an angular resolution of 3.5 arcmin. The unprecedented resolution and sensitivity of the GALFA-H I survey resulted in the detection of numerous isolated, compact H I clouds at low Galactic velocities, which are distinctly separated from the disk H I emission. In the limited area of ∼4600 deg^2 surveyed so far, we have detected 96 such compact clouds. The detected clouds are cold with median $T_{k,\max} \sim 300$ K. Moreover, these clouds are quite compact and faint with median properties of 5 arcmin in angular size, 0.75 K in peak brightness temperature, and $N_{\rm H I}$ of 5×10^{18} cm^{-2}. Most of the clouds deviate from Galactic rotation at the 20–30 km s^{-1} level, and a significant fraction shows evidence for a multiphase medium and/or velocity gradients. No counterparts for these clouds were found in other wave bands.

From the modeling of spatial and velocity distribution of the whole compact cloud population, we find that the bulk of the population is related to the Galactic disk and their distances are likely to be in the range of 0.1 to a few kpc. This is consistent with

distance estimates based on the thermal pressure requirements for the CNM and the WNM coexistence, and the tangent-point method for a subset of clouds.

If the clouds are at a distance ⩽1 kpc, they would represent low-column-density examples of the population of CNM Galactic clouds on sub-parsec scales. Possible mechanisms for the formation of such clouds involve stellar outflows, and/or condensation of the WNM by the collision of turbulent flows. Once formed, such cold, low-column-density, compact H I clouds would evaporate on timescales of ∼Myr due to the combination of conductive heat transfer and/or Kelvin–Helmholtz instabilities from the surrounding warm/hot medium. Conversely, if the clouds are at distances of a few kpc, they are similar to the H I clumps observed in the Galactic disk–halo interface region. One potential mechanism that may be able to explain the existence of such cold clouds was recently proposed by Heitsch & Putman (2009) and involves the recooling of inflowing gas. Finally, our modeling of cloud distributions cannot exclude the possibility of sporadic compact clouds being at large distances. If such clouds are at large distances and self-gravitating, they would be extremely dark matter dominated and may be related to the dark matter mini-halos predicted by cosmological simulations.

Our completeness check of the compact cloud catalog showed that we are most likely missing about one quarter of the clouds due to our selection biases for regions where the Galactic background is below 4 K. In addition, we cannot detect any clouds in regions where the Galactic background exceeds 4 K. We speculate that faint, compact H I clouds are probably widespread throughout the Galaxy, but we are able to detect them only in the regions with low Galactic emission. In the future, by completing the GALFA-H I survey and applying automated methods for cloud detection we will collate a larger sample of compact clouds and extend our latitude coverage to $b \sim 0°$. This will allow us to better constrain cloud spatial distribution through the latitude and velocity modeling discussed in the paper. In addition, we will investigate whether compact clouds are related to local events, such as stellar winds or large-scale atomic flows, or are globally distributed across the disk with notable kinematic properties. To fully study this cloud population, we will have to wait for the next generation radio telescopes (Australian SKA Pathfinder, MeerKAT, or the Square Kilometer Array) which will play an important role in providing a census of compact clouds by providing sensitive and high-resolution surveys, capable of filtering large-scale diffuse H I emission.

REFERENCES

Audit, E., & Hennebelle, P. 2005, A&A, 433, 1
Auld, et al. 2006, MNRAS, 371, 1617
Begum, A., Chengalur, J. N., Karachentsev, I. D., Kaisin, S. S., & Sharina, M. E. 2006, MNRAS, 365, 1220
Begum, A., Chengalur, J. N., Karachentsev, I. D., Sharina, M. E., & Kaisin, S. S. 2008, MNRAS, 386, 1667
Bekhti, B. N., Richter, P., Winkel, B., Kenn, F., & Westmeier, T. 2009, A&A, 503, 483
Braun, R., & Kanekar, N. 2005, A&A, 436, 53L
Clemens, D. P. 1985, ApJ, 295, 422
Collins, J. A., Benjamin, R. A., & Rand, R. J. 2002, ApJ, 578, 98
de Avillez, M. A., & Breitscwerdt, D. 2005, ApJ, 634, L65
Dedes, L., Dedes, C., & Kalberla, P. W. M. 2008, A&A, 491, L45
Dedes, L., & Kalberla, P. W. M. 2010, A&A, 509, A60
Downes, R. A., Webblink, R. F., Shara, M. M., Ritter, H., Kolb, U., & Duerbeck, H. W. 2006, VizieR On-line Data Catalog: V/123A
Field, G. B., Goldsmith, D. W., & Habing, H. J. 1969, ApJ, 155, L149
Ford, A. H., McClure-Griffiths, N. M., Lockman, F. J., Bailin, J., Calabretta, M. R., Kalberla, P. M. W., Murphy, T., & Pisano, D. J. 2008, ApJ, 688, 290
Frail, D. A., Weisberg, J. M., Cordes, J. M., & Mathers, C. 1994, ApJ, 436, 144
Frisch, P. C., Grodnicki, L., & Welty, D. E. 2002, ApJ, 574, 834
Gerard, E., & Le Bertre, T. 2006, AJ, 132, 2566
Gibson, S. J., Taylor, R., Higgs, L. A., Brunt, C. M., & Dewdney, P. E. 2005, ApJ, 626, 195
Giovanelli, R., Haynes, M. P., Kent, B. R., & Adams, E. A. K. 2010, ApJ, 708, 22L
Giovanelli, R., et al. 2005, AJ, 130, 2598
Gooch, R. 1996, in ASP Conf. Ser. 101, Astronomical Data Analysis Software and Systems V, ed. G. H. Jacoby & J. Barnes (San Francisco, CA: ASP), 80
Guram, S. S., & Taylor, A. R. 2009, in ASP Conf. Ser. 407, The Low-Frequency Radio Universe, ed. D. J. Saikia, et al. (San Francisco, CA: ASP), 282
Gussie, G. T., & Taylor, A. R. 1995, MNRAS, 273, 801
Heiles, C. 1997, ApJ, 481, 193
Heiles, C., & Troland, T. H. 2003a, ApJS, 145, 329
Heiles, C., & Troland, T. H. 2003b, ApJ, 586, 1067
Heitsch, F., & Putman, M. E. 2009, ApJ, 698, 1485
Houck, J. C., & Bregman, J. N. 1990, ApJ, 352, 506

Kalberla, P. M. W., Burton, W. B., Hartmann, D., Arnal, E. M., Bajaja, E., Morras, R., & Poppel, W. G. L. 2005, A&A, 440, 775
Kalberla, P. M. W., & Haud, U. 2006, A&A, 455, 481
Kalberla, P. M. W., & Kerp, J. 2009, ARA&A, 47, 27
Klypin, A., Kravtsov, A., Valenzuela, O., & Prada, F. 1999, ApJ, 522, 82
Koyama, H., & Inutsuka, S. 2002, ApJ, 564, L97
Levine, E. S., Heiles, C., & Blitz, L. 2008, ApJ, 679, 1288
Lockman, F. J. 2002, ApJ, 580, L47
Marinacci, F., Fraternalli, F., Ciotti, L., & Nipoti, C. 2010, MNRAS, 401, 2451
Matthews, L. D., Libert, Y., Gerard, E., Le Berte, T., & Reid, M. J. 2008, ApJ, 684, 603
McClure-Griffiths, N. M., et al. 2009, ApJS, 181, 398
McKee, C. F., & Cowie, L. L. 1977, ApJ, 215, 213
McKee, C. F., & Ostriker, J. P. 1977, ApJ, 218, 148
Moore, B., Ghigna, S., Governato, F., Lake, G., Quinn, T., Stadel, J., & Tozzi, P. 1999, ApJ, 524, L19
Muller, H., Frisch, O. C., Florinski, V., & Zank, G. P. 2006, ApJ, 647, 1491
Peek, J. E. G., & Heiles, C. 2008, arXiv:0810.1283
Peek, J. E. G., Heiles, C., Putman, M. E., & Douglas, K. 2009, ApJ, 692, 827
Philips, J. P. 1999, A&AS, 134, 241
Putman, M. E., et al. 2002, AJ, 123, 873
Redfield, S., & Linsky, J. L. 2002, ApJS, 139, 439
Redfield, S., & Linsky, J. L. 2008, ApJ, 673, 283
Rodriguez, L. F., Goss, M. W., & Williams, R. 2002, ApJ, 574, 179
Rosolowsky, E., Engargiola, G., Plambeck, R., & Blitz, L. 2003, ApJ, 599, 258
Ryan-Weber, E. V., Begum, A., Oosterloo, T., Pal, S., Irwin, M. J., Belokurov, V., Evans, N. W., & Zucker, D. B. 2008, MNRAS, 384, 535
Savage, B. D., et al. 2003, ApJS, 146, 125
Schneider, P. 2006, Extragalactic Astronomy and Cosmology: An Introduction (Berlin: Springer)
Stanimirović, S., & Heiles, C. 2005, ApJ, 631, 371
Stanimirović, S., Heiles, C., & Kanekar, N. 2007, in ASP Conf. Ser. 365, SINS—Small Ionized and Neutral Structures in the Diffuse Interstellar Medium, ed. M. Haverkorn & W. M. Goss (San Francisco, CA: ASP), 22
Stanimirović, S., Hoffman, S., Helies, C., Douglas, K. A., Putman, M., & Peek, J. E. G. 2008, ApJ, 680, 276
Stanimirović, S., et al. 2006, ApJ, 653, 1210
Sternberg, A., McKee, C. F., & Wolfire, M. G. 2002, ApJS, 143, 419
Stil, J. M., et al. 2006a, ApJ, 637, 366
Stil, J. M., et al. 2006b, AJ, 132, 1158
Vazquez-Semadeni, E., Ryu, D., Passot, T., Gonzalez, R., & Gazol, A. 2006, ApJ, 643, 245
Wakker, B. P. 1991, A&A, 250, 499
Wakker, B. P. 2001, ApJS, 136, 463
Wakker, B. P. 2004, in High Velocity Clouds, ed. H. van Woerden, B. P. Wakker, U. J. Schwarz, & K. S. de Boer (Astrophysics and Space Science Library, Vol. 312; Dordrecht: Kluwer), 25
Welsh, B. Y., Lallement, R., Vergely, J. L., & Raimond, S. 2010, A&A, 510, 54
Wolfire, M. G., McKee, C. F., Hollenbach, D., & Tielens, A. G. G. M. 2003, ApJ, 587, 278
Wood, B. E., Redfield, S., Linsky, J. L., Mller, H. R., & Zank, G. P. 2005, ApJS, 159, 118